Charge transport mechanisms in inkjet-printed thin-film transistors based on two-dimensional materials

Erik Piatti [1,8], Adrees Arbab [2,3,8], Francesco Galanti [1], Tian Carey [3], Luca Anzi [4], Dahnan Spurling [5], Ahin Roy [5], Ainur Zhussupbekova [5], Kishan A. Patel [4], Jong M. Kim [6], Dario Daghero [1], Roman Sordan [4], Valeria Nicolosi [5], Renato S. Gonnelli [1] and Felice Torrisi [3,7 ✉]

Printed electronics using inks based on graphene and other two-dimensional materials can be used to create large-scale, flexible and wearable devices. However, the complexity of ink formulations and the polycrystalline nature of the resulting thin films have made it difficult to examine charge transport in such devices. Here we report the charge transport mechanisms of surfactant- and solvent-free inkjet-printed thin-film devices based on few-layer graphene (semimetal), molybdenum disulfide (MoS$_2$, semiconductor) and titanium carbide MXene (Ti$_3$C$_2$, metal) by investigating the temperature, gate and magnetic-field dependencies of their electrical conductivity. We find that charge transport in printed few-layer MXene and MoS$_2$ devices is dominated by the intrinsic transport mechanism of the constituent flakes: MXene exhibits a weakly localized 2D metallic behaviour at any temperature, whereas MoS$_2$ behaves as an insulator with a crossover from 3D Mott variable-range hopping to nearest-neighbour hopping around 200 K. Charge transport in printed few-layer graphene devices is dominated by the transport mechanism between different flakes, which exhibit 3D Mott variable-range hopping conduction at any temperature.

Printable inks based on graphene and other two-dimensional (2D) materials could be used to make high-performance, flexible[1–6] and wearable electronics[1,7,8]. Electronic inks from 2D materials (E2D inks) are mixtures of a functional 2D material, stabilizers and rheology modifiers. E2D inks with different electronic properties have been developed to print the different elements of a device: semiconducting or semimetallic inks in the active layer, insulating inks for dielectrics and conducting inks for electrodes.

Large-scale production of E2D inks[2,3] has been reported using solution-processing techniques such as electrochemical exfoliation[9,10] and liquid-phase exfoliation, including shear mixing[11], microfluidization[3,6] and ultrasonication[12–14]. Several printing methods such as inkjet printing[3,4,15], screen printing[6,16], flexographic printing[17] and spray coating[18,19] have been used to fabricate electronic[1,20], optoelectronic[21,22] and photonic[23,24] devices. Drop-on-demand inkjet printing is a particularly promising approach because it works with a wide range of substrates (for example, textile, polymers and silicon) in a mask-less and non-contact deposition mode, as well as offers high resolution (~50 μm) and low material losses (<1 ml)[25].

Inkjet-printed field-effect transistors (FETs) with graphene inks on polyethylene terephthalate (PET) substrates have demonstrated mobilities of up to ~204 cm^2 V^{-1} s^{-1} (ref. [3]), and current modulation has also been achieved using ionic gating with spray-coated hexagonal boron nitride as a porous separator[4]. Inkjet-printed photodetectors[5,26] achieved photoresponsivities of up to ~50 mA W^{-1}, using molybdenum disulfide (MoS$_2$) on polyimide[26]. Although charge transport mechanisms in isolated flakes of 2D materials—including[27]

MoS$_2$[28–31], graphene[32–34] and MXenes[35,36]—have been extensively investigated, the mechanism in inkjet-printed films of E2D inks remains poorly understood. This is because the structure of inkjet-printed films consists of a large number of highly crystalline flakes assembled together in a three-dimensional (3D) network[1], and is more complex than that of isolated flakes. As a result, transport depends on an interplay between charge-carrier propagation within each flake (intra-flake transport) and propagation from one flake to the surrounding flakes in the network (inter-flake transport)[37]. It also introduces additional disorder with respect to that found in isolated flakes in the form of sharp boundaries between the different printed flakes in the network[2]. Previous attempts to probe low-temperature conductivity in printed thin films of semiconducting transition metal dichalcogenides have suggested that charge transport occurs via some kind of hopping mechanism, but have failed to reach a conclusion on the specific model[4].

In this Article, we report the charge transport mechanisms of inkjet-printed field-effect devices by examining the temperature, gate and magnetic-field dependencies of their electrical conductivity. Our printed films are made from surfactant-free titanium carbide (Ti$_3$C$_2$) MXene, MoS$_2$ and graphene inks—representing metallic, semiconducting and semimetallic 2D inks, respectively—and are composed of a network of 2D material flakes. We demonstrate that in the printed MXene and MoS$_2$ devices, charge transport is dominated by intra-flake processes and mirrors that in the isolated constituent flakes. In printed graphene devices, transport is dominated by inter-flake processes and deviates from the semimetallic behaviour of isolated graphene.

[1]Department of Applied Science and Technology, Politecnico di Torino, Torino, Italy. [2]Cambridge Graphene Centre, University of Cambridge, Cambridge, UK. [3]Department of Chemistry, Molecular Sciences Research Hub, Imperial College London, London, UK. [4]L-NESS, Department of Physics, Politecnico di Milano, Como, Italy. [5]Trinity College, Dublin, Ireland. [6]Department of Engineering, University of Cambridge, Cambridge, UK. [7]Dipartimento di Fisica e Astronomia, Universita' di Catania, Via S. Sofia, Catania, Italy. [8]These authors contributed equally: Erik Piatti, Adrees Arbab. ✉e-mail: f.torrisi@imperial.ac.uk
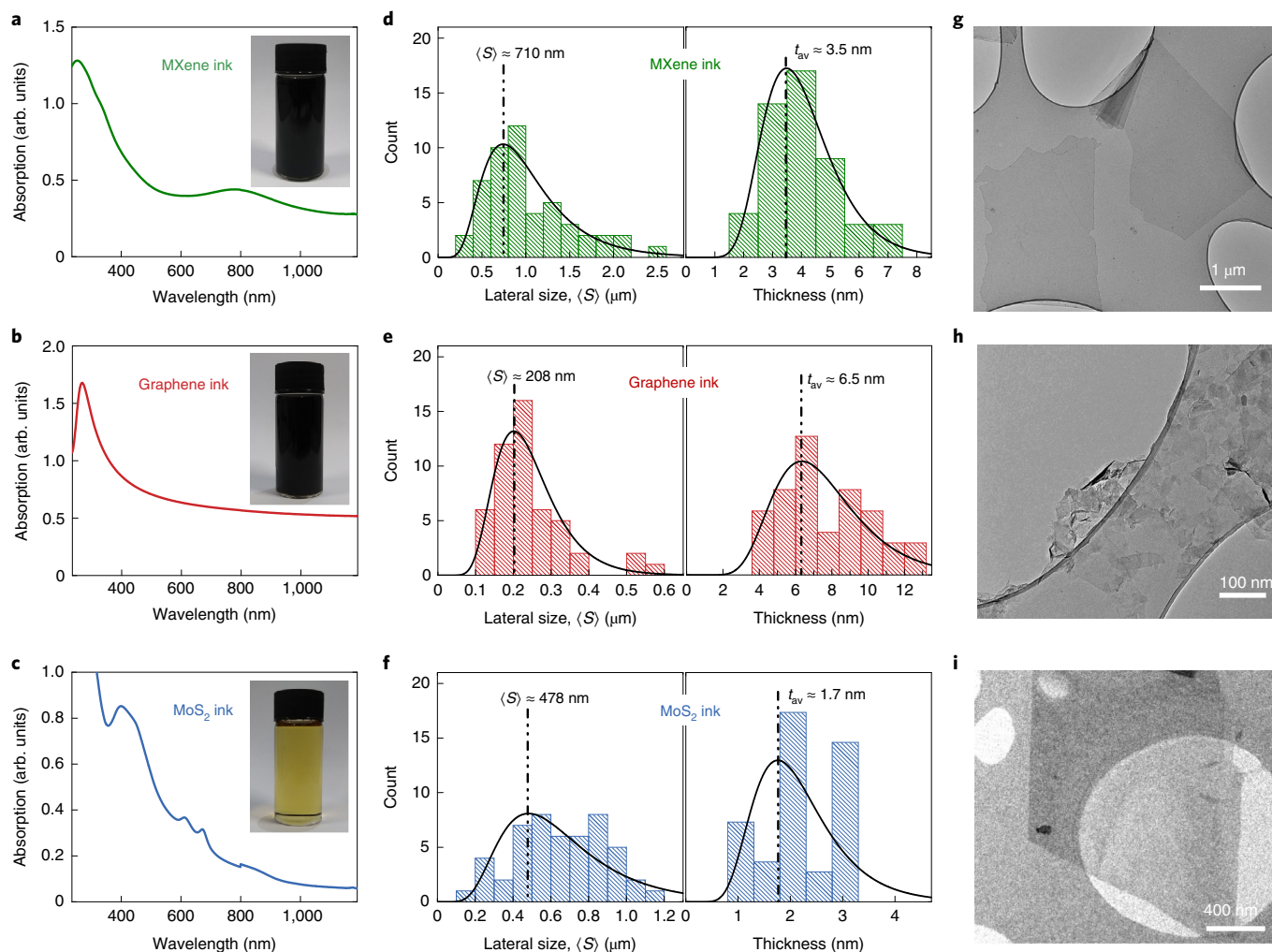
Fig. 1 | UV–vis, AFM and TEM characterization of E2D inks. a–c, Ultraviolet spectroscopy of MXene (**a**), graphene (**b**) and MoS₂ (**c**) inks used to make the thin films. The insets show the photographs of the corresponding solvent-dispersed 2D material flakes. **d–f**, Statistics of the lateral size and thickness of MXene (**d**), graphene (**e**) and MoS₂ (**f**) flakes in E2D inks. **g–i**, TEM image of MXene (**g**), graphene (**h**) and MoS₂ (**i**) flakes in the E2D inks.

Ink formulation and material characterization

Typically, E2D-ink formulations require the use of additives such as binders (substances that cohesively hold materials together) or surfactants, which degrade the electrical properties of the ink[2,3,38] as most of the binders and surfactants hinder the hopping of charge carriers through a film of 2D materials. Solvent-exchange techniques have been successfully adopted on exfoliated layered material dispersions to produce stabilizer-free low-boiling-point (<100 °C) E2D inks in ethanol for use in inkjet-printed electronics[3]. Here we adopt a solvent-exchange technique (Methods) yielding pure graphene, MoS₂ and Ti₃C₂ low-boiling-point inks in ethanol, which is suitable for inkjet printing. The graphene ink was prepared by the ultrasonic exfoliation of graphite (Methods) following our previous work[3]. The MXene ink was produced by etching aluminium (Al) in MAX (Ti₃AlC₂) powder using the in situ hydrofluoric acid method (Methods)[20], whereas the MoS₂ ink was prepared by the electrochemical exfoliation of bulk MoS₂ layered crystals via quaternary ammonium molecules (Methods)[10]. We measure the optical absorption spectra in the ultraviolet–visible (UV–vis) range to estimate flake concentration c via the Beer–Lambert law (Methods) for the MXene (Fig. 1a), graphene (Fig. 1b) and MoS₂ (Fig. 1c) inks. We obtain flake concentration $c_{MX} \approx 0.500$ mg ml⁻¹, $c_{GR} \approx 0.495$ mg ml⁻¹ and $c_{MS} \approx 2.730$ mg ml⁻¹ for the MXene, graphene and MoS₂ inks, respectively. The UV–vis spectrum

of the graphene ink is mostly featureless as expected[39], with a prominent peak at ~268 nm attributable to the Van Hove singularity in the graphene density of states (DOS)[39]. The UV–vis spectrum of the MoS₂ ink shows the characteristic A (~610 nm) and B (~675 nm) excitonic peaks of the 2H semiconducting crystal phase[40], as well as a broader feature at ~420 nm due to the convolution of the C and D excitonic peaks[41]. The UV–vis spectrum of the MXene ink shows a distinct peak at ~260 nm, which originates from surface termination groups (–F, –OH and –O)[42,43], generated during the etching process (Methods)[44]. The MXene ink also has a broad peak at ~800 nm, which is associated to a transversal surface plasmon in the MXene flakes[45–47]; this is greatly enhanced on the functionalization of their surface with Al oxoanion groups[48]. We employ energy-dispersive X-ray spectroscopy (EDX) to confirm the removal of Al from the MAX phase precursor during the etching process to form the MXene ink (Supplementary Fig. 1). The EDX Al signal at ~1 keV is substantially weak compared with that of titanium (Ti) and carbon (C), and comparable to the signal obtained for high-quality Ti₃C₂ MXenes in previous reports[42–44]. We then validate the suitability of these inks for inkjet printing using these parameters to calculate the figure of merit, Z (Methods)[49], finding $Z_{GR} \approx 22$, $Z_{MS} \approx 11$ and $Z_{MX} \approx 4$ for the graphene, MoS₂ and MXene inks, respectively, in accordance with previous reports on inkjet-printed E2D inks[3,15].
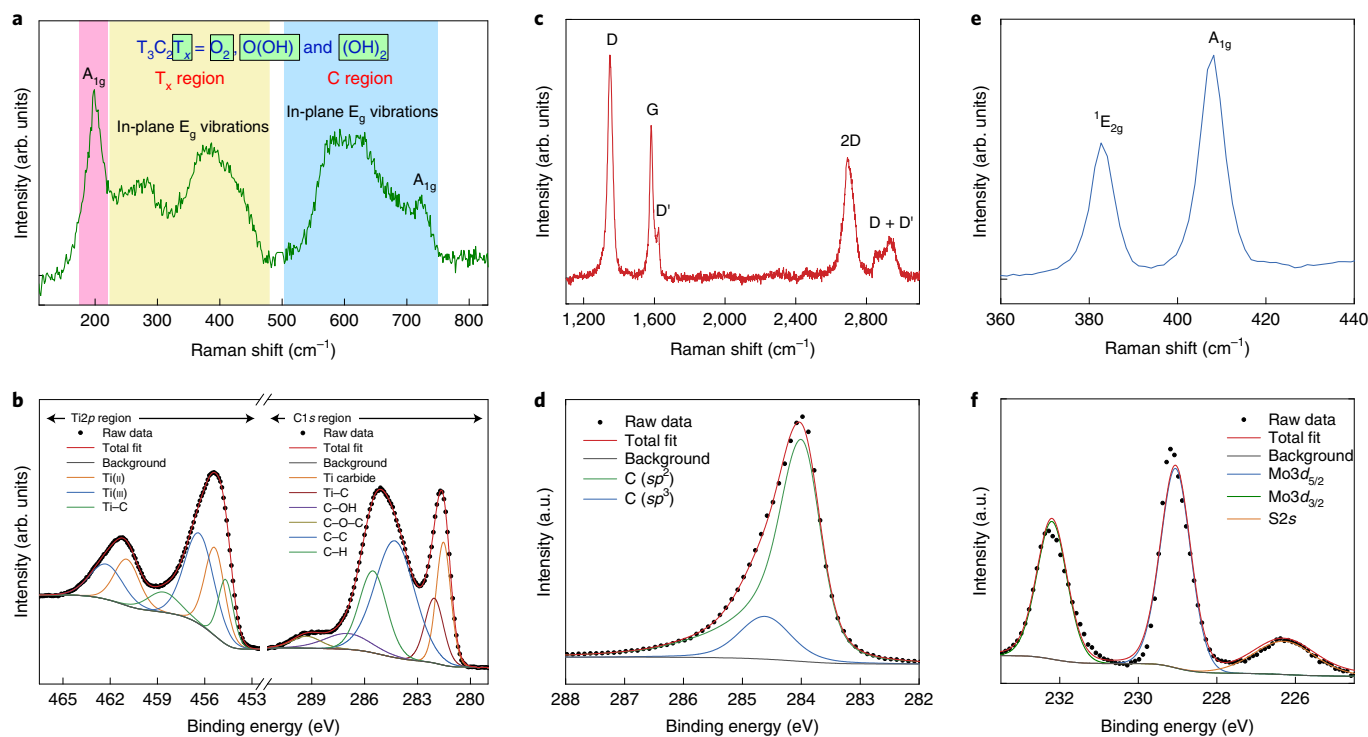
Fig. 2 | Raman spectroscopy and XPS data of E2D inks. a, Raman spectrum of the MXene ink. The blue- and pink-shaded areas indicate the in-plane and out-of-plane modes, respectively, due to either termination groups (T_x region) or C atoms (C region). **b**, XPS data of the MXene ink, showing the C1s and the Ti2p regions. **c,d**, Raman spectrum (**c**) of the graphene ink and its XPS data (**d**), showing the C region comprising sp^2 and sp^3 C atoms. **e,f**, Raman spectra (**e**) of the MoS_2 ink and its XPS data (**f**) showing the Mo region. All the Raman spectra are acquired at 514.5 nm.

Atomic force microscopy (AFM) is used to estimate the lateral size $\langle S \rangle$ and average thickness t_{av} of the 2D material flakes (Methods and Supplementary Figs. 2–4). Figure 1d–f shows the statistical distributions of $\langle S \rangle$ and t_{av} in the form of a histogram for MXene, graphene and MoS_2 inks. A log-normal distribution peaked at $\langle S \rangle_{MX} \approx 710$ nm, $\langle S \rangle_{GR} \approx 208$ nm and $\langle S \rangle_{MS} \approx 478$ nm appears for the MXene, graphene and MoS_2 flakes, respectively. This confirms that the flake dimensions fall within the required range for drop-on-demand inkjet printing[15]. We also find the average flake thickness for the MXene, graphene and MoS_2 inks to be $t_{av,MX} \approx 3.5$ nm, $t_{av,GR} \approx 6.5$ nm and $t_{av,MS} \approx 1.7$ nm. Transmission electron microscopy (TEM) corroborates the distribution of the lateral size of the flakes in the inks (Figs. 1g–i), showing that the MXene inks can have flakes with $\langle S \rangle \geq 1$ μm, whereas graphene and MoS_2 flakes tend to be in the range of $\langle S \rangle \approx 200{-}900$ nm.

We then employ Raman spectroscopy to examine the structural quality of the E2D flakes and X-ray photoelectron spectroscopy (XPS) to assess their stoichiometry (Methods). In the MXene ink, the Raman spectrum (Fig. 2a) shows two broad resonant regions, typical of Ti_3C_2 MXenes (Supplementary Section V), denoted as the T_x region between ~223 and ~480 cm⁻¹ and the C region between ~503 and ~750 cm⁻¹. An additional peak appears at ~205 cm⁻¹ and is caused by an A_{1g} out-of-plane vibrational mode that originates from the C atoms; two Ti layers; and functional –OH, –O and –F surface groups[50]. This is confirmed by the EDX data (Methods) showing the presence of –O and –F and minor traces of –Cl (Supplementary Fig. 1).

Figure 2b shows the XPS data of the C1s and Ti2p regions for the MXene ink, which confirm the formation of Ti_3C_2 from the MAX phase powder. The C1s region comprises six non-doublet peaks belonging to graphitic C–C formation, Ti carbide and Ti–C bonds, C–OH and C–O–C bonds, and C–H functional group on the

surface of the MXene flakes (Supplementary Section VI). The Ti2p region contains three doublet peaks associated with the $Ti_3C_2O_x$ and $Ti_3C_2(HO)$ functional groups on the MXene flake surface[50,51]. The asymmetric Ti–C ($2p_{3/2}$, ~454.8 eV; $2p_{1/2}$, ~460 eV) peak, which is commonly associated with MXene flakes, is shifted to a larger binding energy compared with its precursor MAX phase powder. This is attributed to the Al in the MAX phase powder (Ti–C $2p_{3/2}$, ~454.6 eV) being replaced by a more electronegative termination group like –F, –O and –OH (refs. [51–54]).

The Raman spectrum of the graphene ink (Fig. 2c) shows the characteristic G and D peaks at ~1,581 and ~1,349 cm⁻¹, respectively. In addition, a D + D′ peak and a Lorentzian-shaped 2D peak are positioned at ~2,950 cm⁻¹ and ~2,700 cm⁻¹, respectively. These indicate that the graphene film comprises electronically decoupled graphene layers (Methods). In pristine graphene inks, the D peak corresponds to the flake edges rather than to the presence of a disorder within the flakes[15,55]. The D + D′ peak is attributed to a two-photon defect-assisted process[55]. The XPS data of the graphene ink (Fig. 2d) show a convoluted peak, composed of two peaks associated with sp^2 and sp^3 C atoms[56]. The sp^2 peak (green curve) at ~283.9 eV has a broad and asymmetric tail at higher binding energies, which is not present in the case of the sp^3 peak (blue curve) at ~284.7 eV. Integrating the area under the two curves reveals a ratio of 80%:20% (sp^2:sp^3), which implies that the majority of C atoms are sp^2 hybridized (Methods).

In the MoS_2 ink, the Raman spectrum (Fig. 2e) shows the typical $^1E_{2g}$ and A_{1g} peaks that appear at ~382.5 and ~407.0 cm⁻¹, respectively. The position of both peaks indicates the high crystallinity of the flakes[57]. Figure 2f shows the XPS data of the MoS_2 inks, which exhibit $3d_{3/2}$ and $3d_{5/2}$ doublet peaks associated with molybdenum (Mo) that appear at ~232 and ~229 eV, respectively. The XPS data also show a 2s peak originating from the sulfur (S) atoms in MoS_2[58].
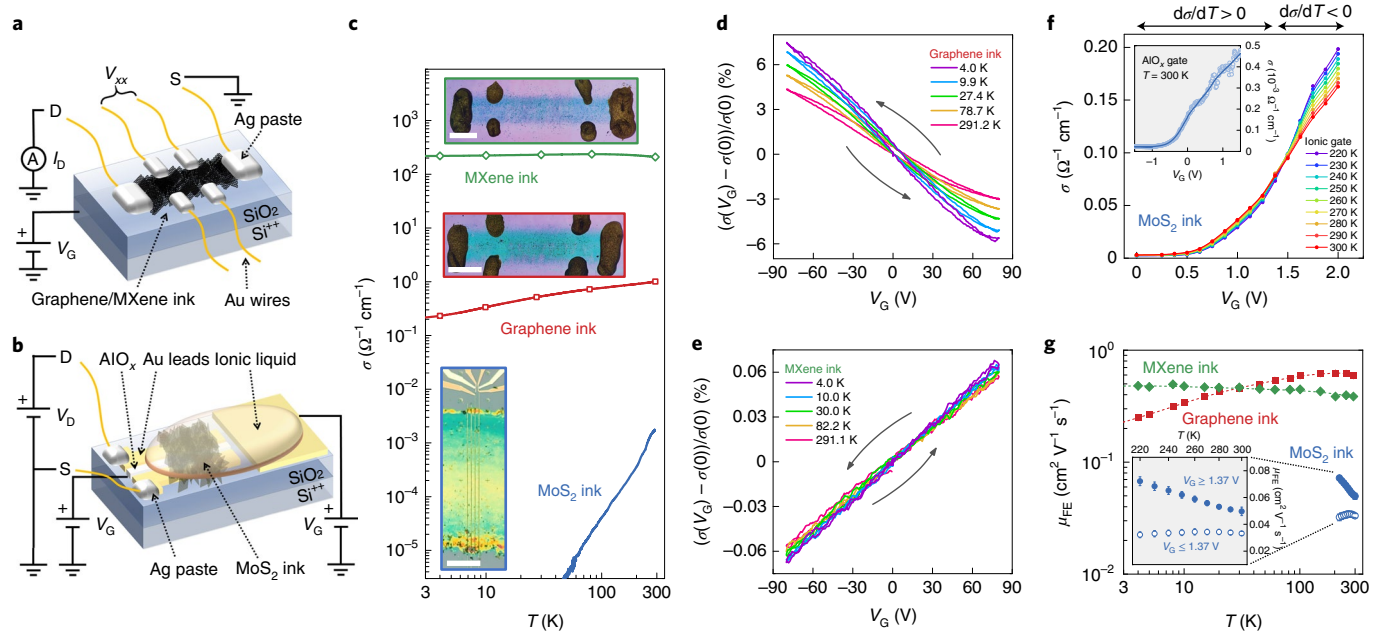
Fig. 3 | Charge transport measurements in E2D-ink transistors. a,b, Sketch of an inkjet-printed graphene/MXene field-effect device (**a**) and an inkjet-printed MoS$_2$ device (**b**). S, source; D, drain. **c**, Conductivity σ at gate voltage $V_G = 0$ as a function of temperature T in E2D-ink FETs, in the double logarithmic scale. The solid blue, red and green lines are the σ values of the printed MoS$_2$-ink device, printed graphene-ink device and printed MXene-ink device, respectively. The hollow symbols are the values of $\sigma(0)$ for which the V_G sweeps are shown in **d** and **e**. The insets show the optical images of the printed MXene-ink device (green border; scale bar, 4 mm), printed graphene-ink device (red border; scale bar, 4 mm) and printed MoS$_2$-ink device (blue border; scale bar, 100 μm). **d,e**, Conductivity ratio $[\sigma(V_G) - \sigma(0)]/\sigma(0)$ as a function of V_G for increasing T in the printed graphene-ink device (**d**) and printed MXene-ink device (**e**). The black arrows indicate the direction of V_G sweeps. **f**, The σ value of the printed MoS$_2$-ink device as a function of V_G applied to the ionic gate at different temperatures, constructed by starting from the curves of σ as a function of T at different V_G values shown in Fig. 4c. The inset shows σ as a function of V_G applied through AlO$_x$ via the Al gate electrode. **g**, Field-effect mobility μ_{FE} as a function of T in the logarithmic scale for the printed graphene-ink device (red squares), printed MXene-ink device (green diamonds) and printed MoS$_2$-ink device (hollow blue circles, $V_G \leq 1.37$ V; filled blue circles, $V_G \geq 1.37$ V). The dashed lines are guides to the eye. The inset shows a magnification of MoS$_2$ mobility in the linear scale. Error bars in panel g are the statistical uncertainty on the linear fits (Methods).

Inkjet-printed 2D material thin-film devices

We fabricate the graphene and MXene thin-film devices by inkjet printing the graphene and MXene inks on p-doped Si/SiO$_2$ substrates and the MoS$_2$ thin-film devices by inkjet printing the MoS$_2$ ink on a pre-patterned substrate (Methods). We additionally fabricate flexible graphene films on PET (as detailed elsewhere[3]) for comparison. The low boiling point of our E2D inks improves morphological uniformity and assists in solvent removal after printing[18]. When undertaking inkjet printing, the ejected drop contacts the substrate (as discussed in Supplementary Section VII and Supplementary Figs. 5 and 6), followed by annealing (Methods). AFM and profilometer data show that the rectangular printed films of graphene, MXene and MoS$_2$ inks have a thickness of $t_{d,GR} \approx 130$ nm, $t_{d,MX} \approx 30$ nm and $t_{d,MS} \approx 40$ nm (Supplementary Figs. 2–4), respectively, which were selected to ensure that the percolation threshold for each E2D ink is achieved[59].

The inkjet-printed thin-film devices were then contacted for charge transport measurements (Methods), as shown by the schematic in Fig. 3a,b for graphene/MXene and MoS$_2$ devices, respectively. Figure 3c plots conductivity σ as a function of temperature T for the inkjet-printed MXene, graphene and MoS$_2$ thin-film devices at a gate voltage $V_G = 0$ (green, red and blue curves, respectively; Methods). At $T = 290$ K, the conductivity of the inkjet-printed devices spans over five orders of magnitude, ranging from $\sigma_{MS} = 1.7 \times 10^{-3}$ Ω^{-1} cm^{-1} in the MoS$_2$-ink device and $\sigma_{GR} = 1.1$ Ω^{-1} cm^{-1} in the graphene-ink device to $\sigma_{MX} = 208$ Ω^{-1} cm^{-1} in the MXene-ink device. Between $T \approx 290$ and 50 K, σ_{MS} decreases by three orders of magnitude, consistent with the behaviour of

ungated MoS$_2$ flakes[28–31], and it falls below 3×10^{-6} Ω^{-1} cm^{-1} for $T \leq 50$ K. In the same T range, σ_{GR} also decreases with decreasing T, although only by a factor of ~5 between $T \approx 290$ and 5 K. These dependencies suggest that charge transport in both MoS$_2$-ink and graphene-ink devices occurs via hopping processes[60–62]. Inter-flake hopping is dominant in the graphene ink, since single flakes typically display a metallic-like behaviour[32–34], which is contrary to that observed in our films. In the MoS$_2$-ink device, single flakes display an insulating-like behaviour; hence, a more comprehensive analysis is needed to understand whether inter- or intra-flake hopping mechanisms dominate. Conversely, σ_{MX} appears to be nearly independent of T in the scale shown in Fig. 3c, in line with reports on MXene epitaxial films[63]; this indicates that charge transport in MXene-ink devices should, thus, occur over extended states[60–62].

Figure 3d,e shows the V_G-dependent conductivity ratio $[\sigma(V_G) - \sigma(0)]/\sigma(0)$ for a subset of T values for the graphene and MXene devices (Supplementary Fig. 7 shows the full set of σ versus V_G curves); $\sigma(0)$ is shown as hollow symbols in Fig. 3c. Here σ_{GR} (Fig. 3d) decreases monotonically with increasing V_G, indicating intrinsic hole conduction induced by the unintentional doping of adsorbed molecules[64]. A finite hysteresis suggests charge transfer with traps close to the graphene–SiO$_2$ interface[64]. Both features are typical of inkjet-printed graphene transistors[3,15]. The maximum gate-induced modulation of σ_{GR} increases as T decreases, going from 7.5% at $T \approx 290$ K to 13.5% at $T \approx 4$ K, remaining smaller but in line with reported modulations in inkjet-printed graphene FETs[3,15,65]. Also, σ_{MX} (Fig. 3e) increases monotonically with increasing V_G, indicating intrinsic electron conduction, without any hysteresis. Both

findings are in agreement with the FET behaviour of single-layer MXene flakes[35,36]. The maximum gate-induced modulation of σ_{MX} slightly increases as T decreases, going from ~0.11% at $T \approx 290$ K to ~0.14% at $T \approx 4$ K, about two orders of magnitude smaller than that of graphene devices and consistent with a metallic behaviour. The modulation is also small compared with that reported in single-layer MXene FETs (~1%) (refs. [35,36]) due to the much larger thickness of our printed films. In the printed MoS_2 devices, we first measured σ as a function of V_G applied through the Al/AlO$_x$ gate stack at $T \approx 300$ K (Fig. 3f, inset). Moreover, σ_{MS} increases monotonically with V_G, indicating an n-type behaviour, on–off ratio of ~25 and mobility of up to ~10^{-1} cm^2 V^{-1} s^{-1}, in line with our recent results[66]. Below $T \approx 300$ K, the response of σ_{MS} to the dielectric gating proved weak and we consequently switched to the ionic gate (Methods). At ~300 K, the ionic-gate-induced modulation of σ_{MS} exhibits n-type behaviour with an on–off ratio of ~50 (Fig. 3f), twice that induced by the solid-oxide gate; it increases to ~85 as T is lowered to 220 K. For $V_G \leq 1.37$ V, σ_{MS} increases with T, similar to the ungated case (Fig. 3c), whereas an opposite dependence of σ_{MS} occurs for $V_G \geq 1.37$ V. The occurrence of a gate-induced crossover from hopping transport over the localized states to band-like transport over the extended states in suggested above $T \approx 220$ K.

Figure 3g shows the field-effect mobility (Methods) as a function of T for the MoS_2 device ($\mu_{FE,MS}$; blue circles), graphene device ($\mu_{FE,GR}$; red squares) and MXene device ($\mu_{FE,MX}$; green diamonds). Here $\mu_{FE,GR}$ decreases from ~0.6 to ~0.2 cm^2 V^{-1} s^{-1} when the device is cooled from $T \approx 290$ to ~4 K, whereas $\mu_{FE,MX}$ slightly increases from ~0.4 to ~0.5 cm^2 V^{-1} s^{-1} in the same T range, consistent with the Hall effect measurements at low T (Supplementary Fig. 8). The values of $\mu_{FE,MX}$ are in good agreement with those reported for both single-layer MXene FETs (0.6–2.6 cm^2 V^{-1} s^{-1})[35,36] and thicker MXene films (0.9–1 cm^2 V^{-1} s^{-1})[45,67]. The weak increase in $\mu_{FE,MX}$ as T decreases is typical of disordered metallic systems where the main source of charge-carrier scattering comes from defects[60,61]. The values of $\mu_{FE,GR}$ are instead lower than those reported for inkjet-printed graphene FETs on PET[3], possibly due to the more regular flake arrangement in the graphene films printed on a PET substrate[3] compared with films printed on SiO$_2$. This correlation with the morphology of the system is consistent with the conduction in graphene films being dominated by inter-flake resistance. The monotonic increase in $\mu_{FE,GR}$ with increasing T below 200 K is expected when charge transport occurs via hopping processes[28,68], whereas the saturation and slight decrease in $\mu_{FE,GR}$ between $T \approx 200$ and 290 K suggest a non-negligible impact of electron–phonon (e–ph) scattering in this higher T range[28,32,33]. The values of $\mu_{FE,MS}$ are separately determined in the hopping (Fig. 3g, hollow circles) and band-like (Fig. 3g, filled circles) conduction regions above and below $V_G \approx 1.37$ V (Methods): $\mu_{FE,MS}$ slightly decreases from ~0.034 to ~0.032 cm^2 V^{-1} s^{-1} for $V_G \leq 1.37$ V and $\mu_{FE,MS}$ increases from ~0.049 to ~0.072 cm^2 V^{-1} s^{-1} for $V_G \geq 1.37$ V. These values are in agreement with those determined in the same devices in the absence of the ionic liquid (up to ~10^{-1} cm^2 V^{-1} s^{-1}) and with those recently reported for inkjet-printed MoS_2 FETs[66] and ion-gated MoS_2 networks (0.01–0.10 cm^2 V^{-1} s^{-1}) (refs. [4,69]). The opposite T dependencies exhibited above and below $V_G \approx 1.37$ V again suggest a crossover from hopping transport at low V_G to a band-like one at high V_G, similar to the behaviour reported in disordered, isolated MoS_2 flakes[28].

Charge transport mechanisms

The charge transport mechanisms in our inkjet-printed E2D-ink devices can be determined by making use of robust models originally developed for disordered crystalline materials[60,61] and lately validated for various granular systems[62] including 2D material networks[65,69–72]. These describe charge transport in two distinct regimes—insulating (hopping transport) and metallic (transport over extended states)—separated by the insulator-to-metal transition

(IMT)[60,61] governed by the ratio of intra- and inter-flake conductances[62] (Supplementary Section X). Note that structural parameters like flake size and thickness, degree of overlap, and flake orientation are expected to be of primary importance in the description of granular systems, mainly affecting the absolute value of conductivity, rather than its temperature dependence, on which our analysis will be focused.

Hopping transport in inkjet-printed MoS_2 devices

The electrical conductivity in any hopping regime follows a temperature dependence of the type[60–62]

$$\sigma(T) = \sigma_0 \ \exp\left[-\left(\frac{T_0}{T}\right)^p\right], \tag{1}$$

where T_0 is the characteristic temperature, σ_0 is the conductivity for $T \to \infty$ and p is an exponent that depends on the specific type of hopping mechanism. For the nearest-neighbour hopping (NNH) mechanism, $p = 1$ and σ follows an activated behaviour with activation energy $E_a = k_B T_0$ (refs. [60,61]), where k_B is the Boltzmann constant. All variable-range hopping (VRH) mechanisms instead exhibit $p < 1$, where the Efros–Shklovskii VRH mechanism (ES-VRH) is characterized by $p = 1/2$ (meaning that a soft gap is opened in the DOS at the Fermi level[60–62]) and the Mott VRH mechanism exhibits $p = 1/(1 + d)$, where d is the dimensionality of the system[60–62].

Figure 4a shows σ_{MS} as a function of $T^{-1/4}$ in a representative MoS_2 device in the absence of V_G (ungated): $\log(\sigma_{MS})$ scales linearly with $T^{-1/4}$ for $T \leq 200$ K, indicating 3D Mott VRH conduction[60–62]. ES-VRH, characterized by a $T^{-1/2}$ scaling of $\log(\sigma)$, is instead ruled out (Supplementary Fig. 9). This is further confirmed by determining the reduced activation energy[72,73] as

$$W(T) = \frac{\partial(\ln(\sigma))}{\partial(\ln(T))}. \tag{2}$$

Figure 4b shows the values of $\ln(W_{MS})$ for our MoS_2 device as a function of $\ln(T)$ (circles), and their linear fit for $\ln(T) \leq 5.3$ (dashed line) gives $p_{MS} = 0.23 \pm 0.05$, in good agreement with $p = 1/4$ expected for 3D Mott VRH.

On increasing T above 200 K, $\ln(W_{MS})$ shows a peak and then decreases faster than that below 200 K, leading to $p_{MS} \geq 1$ and the onset of a different transport mechanism. For $T \geq 200$ K, $\log(\sigma_{MS})$ (Fig. 4c, circles) scales with T^{-1} (Fig. 4c), indicating that the electrical conduction occurs via NNH[60,61]. Similar crossovers from Mott VRH at low T to NNH at high T have been reported in disordered MoS_2 flakes[28,31], although the VRH mechanism was invariably of the 2D Mott type[28,30,31,73]. Fitting σ_{MS} in the NNH region to equation (1) with $p = 1$ (Fig. 4c, dashed line) gives $E_{a,MS} = 96.1 \pm 0.5$ meV for our ungated MoS_2 device. Figure 4c also displays σ_{MS} for different values of V_G, and fitting these curves gives the V_G dependence of $E_{a,MS}$, which ranges between ~4 and ~40 meV (Fig. 4d, blue circles). A positive $E_{a,MS}$ is obtained only for V_G up to 1.37 V, since for larger values of V_G, σ_{MS} decreases with increasing T and a negative $E_{a,MS}$ is obtained, which is again consistent with charge transport occurring over extended states for $V_G \geq 1.37$ V and $T \geq 200$ K. The values of $E_{a,MS}$ in both our ungated and gated devices are comparable to those obtained in disordered, isolated MoS_2 flakes[28,31] rather than to the much larger ones obtained in MoS_2 networks[69] where the conduction is dominated by inter-flake hopping (Fig. 4d, grey symbols).

We then determine the localization length ξ_{loc} and average hopping distance R_{hop} in the VRH regime as a function of T (equation 6 and Methods) and compare them with the average thickness of MoS_2 flakes, $t_{av,MS}$ (Fig. 4a, inset). We obtain $\xi_{loc,MS} = 0.21 \pm 0.04$ nm (filled circles), a value smaller than those found in ungated individual MoS_2 flakes, which range between 0.6 and 3.4 nm (refs. [28,31,73]). This is consistent with the stronger insulating behaviour exhibited by our
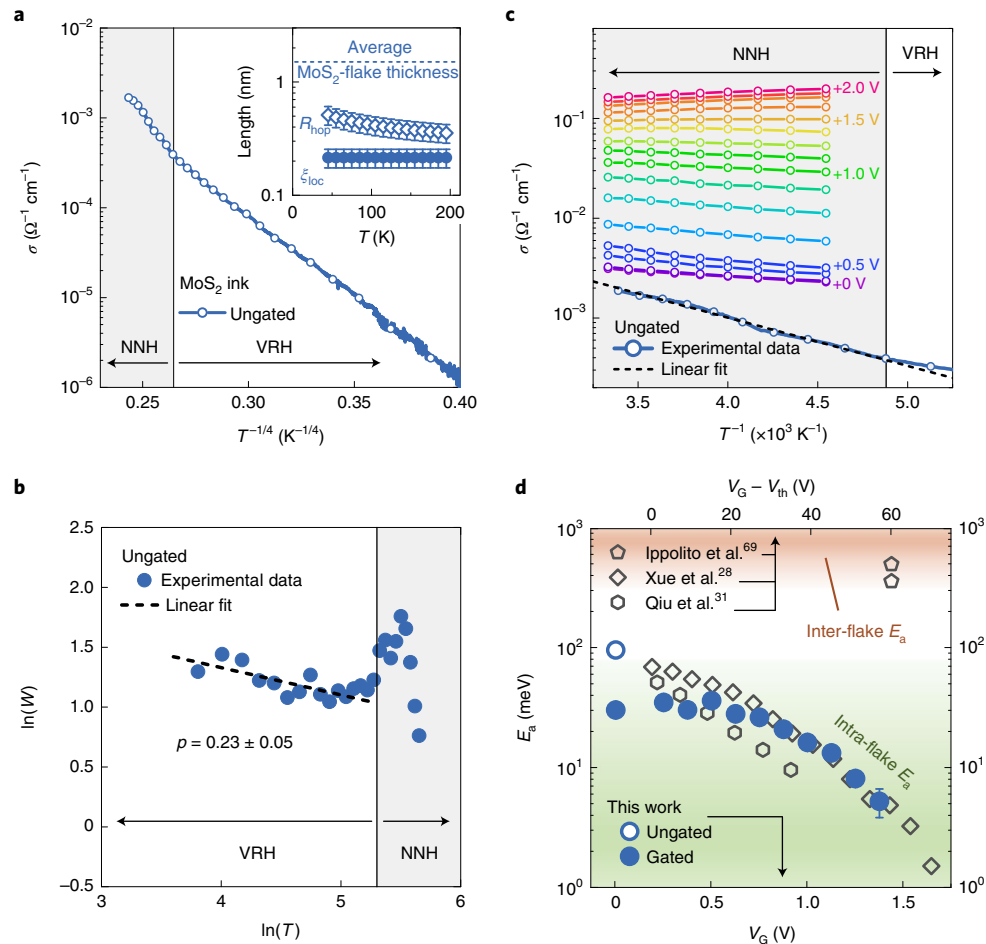
Fig. 4 | Intra-flake hopping transport in printed MoS$_2$ devices. a, Conductivity σ as a function of $T^{-1/4}$ for an ungated MoS$_2$ device (blue solid line). The hollow symbols indicate the data points used to determine the reduced activation energy W shown in **b**. The grey-shaded region highlights the T range ($T \geq 200$ K), where σ deviates from the $T^{-1/4}$ scaling due to the onset of NNH conduction. Inset: localization length ξ_{loc} (filled circles) and average hopping distance R_{hop} (hollow diamonds) as a function of T. The lengths are obtained by combining the T dependence of σ with the estimated values of $N(E_F)$ using equation (6). The horizontal dashed line highlights the average flake thickness in the MoS$_2$ ink. The error bars in Fig. 4a are obtained by standard error propagation in Eqs. 6, 7 from the errors of T_0 and E_a (Methods). **b**, Values of $\ln(W)$ as a function of $\ln(T)$ extracted from the numerical derivation of the data shown in **a**. The dashed black line is the linear fit to the data in the range of $\ln(T) \leq 5$, which allows determining the corresponding value of the scaling exponent p. **c**, Values of σ as a function of T^{-1} for different values of gate voltage V_G. The circles indicate the points used to determine the transfer curves in Fig. 3f. The blue curve refers to the ungated device, and the dashed black line is the linear fit to these data for $T \geq 200$ K, that is, in the NNH regime (grey-shaded region). **d**, Activation energy E_a as a function of V_G (bottom axis) in different MoS$_2$ devices. The blue circles are obtained from the fit of the conductance curves in **c**. The black symbols are the values of E_a reported in disordered MoS$_2$ flakes (diamonds[28] and hexagons[31]) and in MoS$_2$ networks (pentagons[69]) as a function of the difference between the solid-gate voltage and threshold voltage (V_{th}) for electronic conduction (top axis).

printed MoS$_2$ devices, as also shown by $T_{0,MS} = (3.07 \pm 0.10) \times 10^6$ K (Methods) being one order of magnitude larger than the values reported in ungated individual MoS$_2$ nanoflakes[28,31]. Here $R_{hop,MS}$ (hollow diamonds in fig. 4a) ranges from ~0.3 nm at 200 K to ~0.5 nm at 45 K, thus remaining smaller than $t_{av,MS}$ in the entire T range. On average, an electron will, therefore, hop multiple times before being able to escape each MoS$_2$ flake in the out-of-plane direction, accounting for how a 3D VRH can be observed even when the flakes are quasi-2D and the rate-limiting step is intra-flake hopping, consistent with the observed values of $E_{a,MS}$. This picture is in agreement with the observed distribution of flake orientations in the MoS$_2$ device (Supplementary Fig. 10), which demonstrates a fairly good alignment to the SiO$_2$ substrate, with a small average relative inclination of $\theta_{MS} < 3°$. This, together with the rather large lateral size of the flakes and their small average thickness, suggests an inkjet-printed film with a high degree of alignment between the MoS$_2$ flakes with good inter-flake connectivity in

which, however, the conductivity is dominated by an intra-flake mechanism of conduction.

Overall, the charge transport in our inkjet-printed MoS$_2$ devices is dominated by intra-flake hopping processes. Ungated devices sit deep in the insulating side of the IMT, and exhibit a crossover from 3D Mott VRH conduction for $T \leq 200$ K to NNH conduction for $T \geq 200$ K. Gated devices, on the other hand, exhibit NNH conduction for $T \geq 200$ K up to $V_G \approx 1.37$ V, and an incipient crossover to high-T conduction over extended states for larger values of V_G.

Hopping transport in inkjet-printed graphene devices

The increase in σ_{GR} with T in printed graphene devices is qualitatively different from the behaviour of isolated graphene flakes, intuitively suggesting that the bottleneck for electronic transport is inter-flake hopping. Figure 5a shows that $\log(\sigma_{GR})$ scales linearly with $T^{-1/4}$ for $V_G = 0$, +80 and −80 V (red, green and brown curves, respectively) up to $T \approx 290$ K, again meaning that a 3D Mott VRH
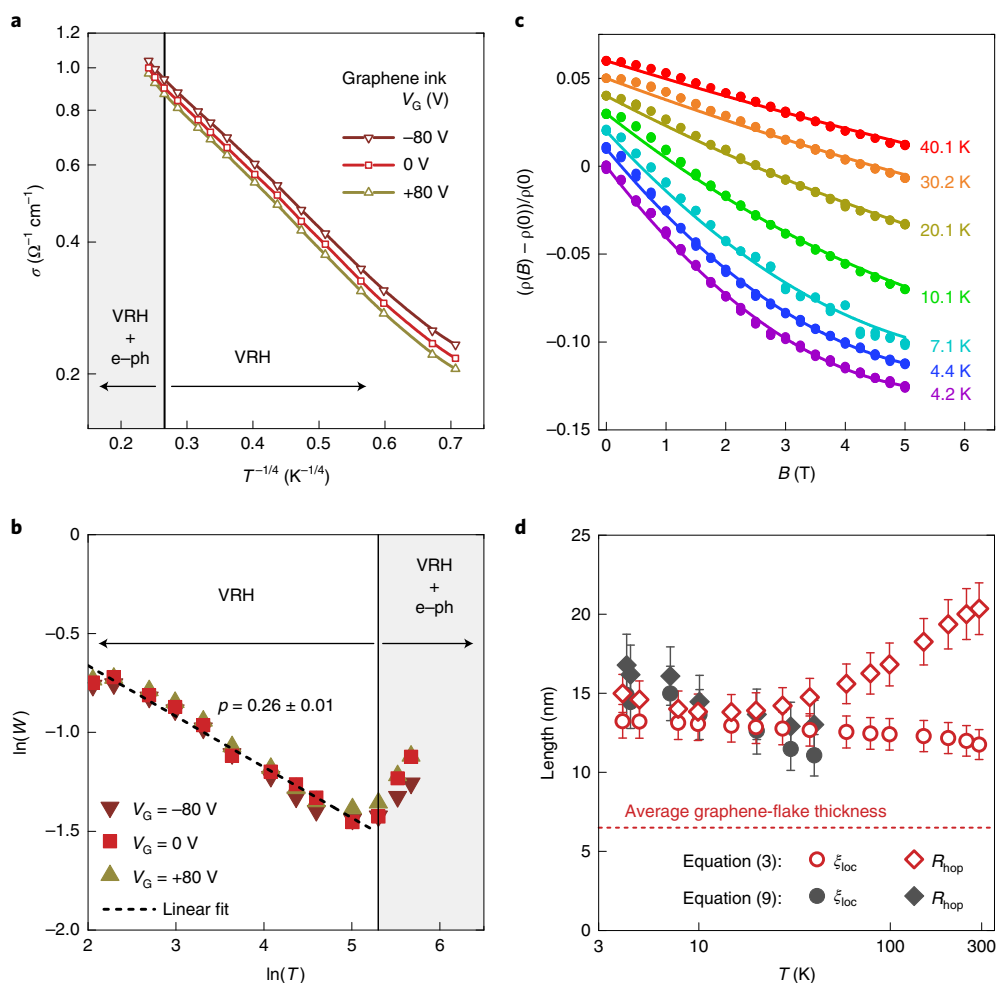
Fig. 5 | Inter-flake hopping transport in printed graphene devices. a, Conductivity σ as a function of $T^{-1/4}$ for a printed graphene device at $V_G = -80$ V (brown solid line with hollow down triangles), $V_G = 0$ V (red solid line with hollow squares) and $V_G = +80$ V (yellow solid line with hollow up triangles). The hollow symbols are data points used to determine the reduced activation energy W shown in **b**. The grey-shaded region highlights the T range where a non-negligible contribution from e–ph scattering is present. **b**, Values of $\ln(W)$ as a function of $\ln(T)$ extracted from the numerical derivation of the data shown in **a**. The dashed black line is the linear fit to the data in the range $2 \leq \ln(T) \leq 5$, which allows to determine the corresponding values of scaling exponent p. **c**, MR as a function of magnetic field B at different temperatures. The filled circles are the experimental data and the solid lines are the fits according to equation (9). Curves at different T values are vertically offset by 0.01 for clarity. **d**, Localization length ξ_{loc} (circles) and average hopping distance R_{hop} (diamonds) as a function of T in the printed graphene device. The lengths indicated with red hollow symbols are obtained by combining the T dependence of σ with the estimated values of $N(E_F)$ using equation (6); those indicated by black filled symbols are instead obtained by combining the T dependence of σ with the MR fits of **c** using equation (9). The horizontal line highlights the average flake thickness in the graphene ink.

mechanism[60–62] is at play over the entire T range. Fitting the data to equation (1) with $p = 1/4$ gives $T_{0,GR} = 138 \pm 11$ K, which is lower than room temperature. This is commonly observed in networks composed of metallic grains when charge transport is dominated by insulating inter-grain hopping[62,70,74], and indicates that the printed graphene device is very close to the IMT[74,75]. Indeed, in granular systems, the inter-grain energy barrier is set by the presence of a finite inter-grain capacitance, and the VRH behaviour can be observed when electrostatic disorder lifts the Coulomb blockade and leads to a finite DOS at the Fermi level[62]. The T dependence of $\log(\sigma_{GR})$ is also incompatible with the $T^{-1/2}$ scaling of ES-VRH (Supplementary Fig. 9). Therefore, the 3D Mott VRH mechanism observed in our devices differs from the hopping behaviour reported in defective graphene (falling either in the ES-VRH regime[76] or in the 2D Mott VRH regime[77,78]) but also from the metallic behaviour usually exhibited by crystalline single- and few-layer graphene flakes[32–34], hopping behaviour observed in inkjet-printed graphene/polymer composites (where NNH dominated by inter-flake capacitive

charging)[65,79] and spin-coated reduced graphene oxide (dominated by ES-VRH)[72].

Figure 5b shows $\ln(W_{GR})$ as a function of $\ln(T)$ for $V_G = 0, +80$ and -80 V (red, green and brown symbols, respectively), which is not monotonic and displays a slope change at $\ln(T) \approx 5.3$ ($T \approx 200$ K). Linearly fitting the data for $2 \leq \ln(T) \leq 5$ (dashed line) gives $p_{GR} = 0.26 \pm 0.01$ irrespective of V_G. Above 200 K, that is, $\ln(T) \geq 5.3$, W_{GR} increases with increasing T, indicating that charge transport deviates from pure VRH scaling, as already suggested by $\mu_{FE,GR}$ decreasing with T in the same T range (Fig. 3g). Therefore, $T \geq 200$ K marks the range where σ_{GR} is no longer purely limited by the carrier hopping probability and e–ph scattering is no longer negligible[32,33]. The dimensionality of VRH in graphene devices is affected by flake orientation: devices printed on SiO_2 display 3D VRH and feature a rather large average relative inclination of flakes with respect to the substrate ($\theta_{GR} \sim 14°$; Supplementary Fig. 10). Instead, flexible graphene films printed on PET exhibit 2D VRH with $p_{GR} = 0.38 \pm 0.02$ (Supplementary Fig. 11) and cross-sectional
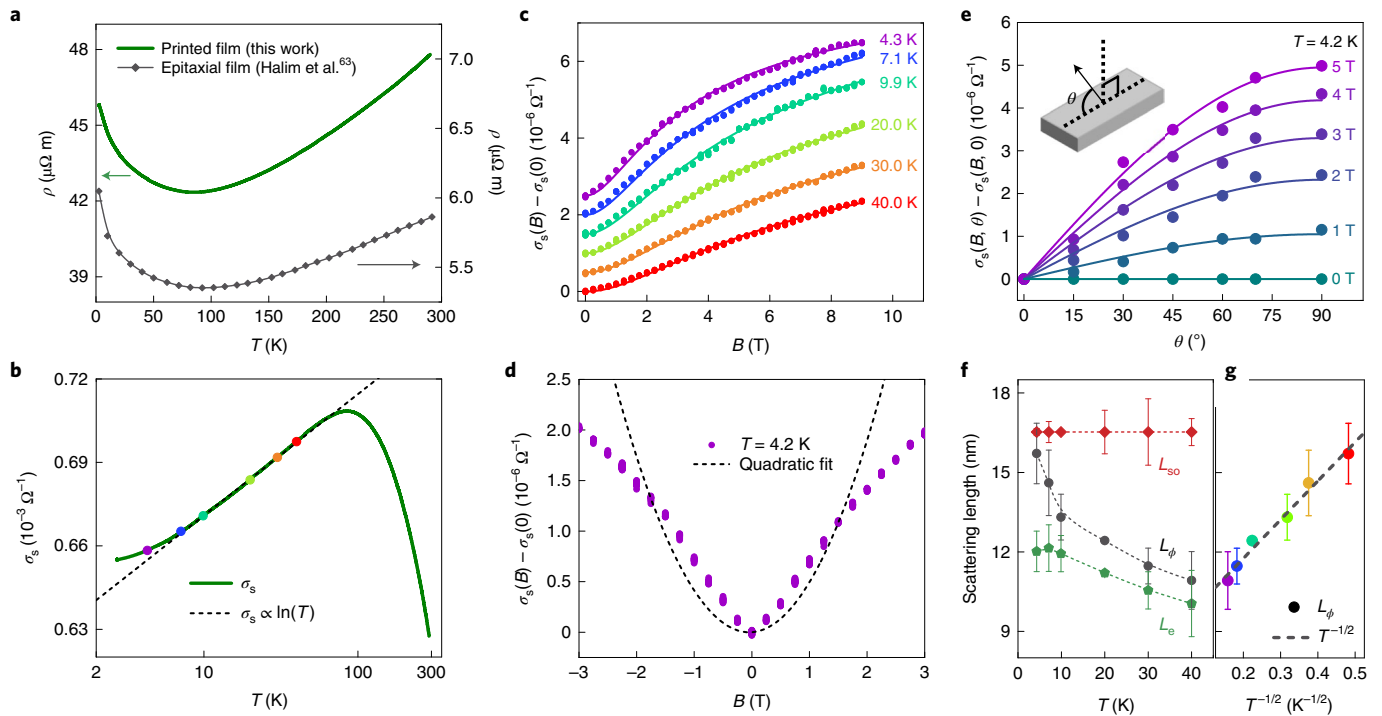
Fig. 6 | Intra-flake metallic transport in printed MXene devices. a, Resistivity ρ as a function of T for a printed MXene device (solid green line; left axis) compared with that of an epitaxial MXene film studied elsewhere[63] (black solid line with filled diamonds; right axis). **b**, Same data of **a** for the printed MXene device, plotted as conductivity per unit surface σ_s as a function of log(T) (solid green line). The dashed black line is a linear fit to the data. The filled coloured circles mark the values of T at which B sweeps shown in **c** were acquired. **c**, Magnetoconductance $\sigma_{2D}(B) - \sigma_{2D}(0)$ as a function of intensity of magnetic field B (perpendicular to the film) for increasing temperatures. The filled circles are experimental data and the solid lines are fits according to equation (12). The curves at different T values are vertically shifted by $5 \times 10^{-7} \Omega^{-1}$ for clarity. **d**, $\sigma_{2D}(B) - \sigma_{2D}(0)$ as a function of B (perpendicular to the film) for low positive and negative values of B. The violet circles are the experimental data at $T = 4.3$ K and the dashed black line is a quadratic fit to the data for $-2 \leq B \leq +2$ T. **e**, Anisotropic magnetoconductance as a function of angle θ between B and substrate plane, for different values of B. The filled circles are the experimental data at $T = 4.2$ K. The solid lines are fits to sin(θ) dependencies. **f**, Spin–orbit length L_{so} (red diamonds), phase-coherence length L_ϕ (black circles) and elastic scattering length L_e (green pentagons) as a function of T, as determined from the fits to equation (12) shown in **c**. The dashed lines are guides to the eye. **g**, L_ϕ as a function of $T^{-1/2}$ (filled coloured circles) and a linear fit to the data (dashed black line). Error bars in **f**, **g** are the statistical uncertainty obtained from the fits to equation (12) shown in **c** (Methods).

TEM analysis shows their flake stacking having a more pronounced in-plane orientation (Supplementary Fig. 12). Thus, the geometry of the printed flake network sets the dimensionality of VRH processes, meaning that inter-flake hopping dominates the conduction process in inkjet-printed graphene devices.

This picture is further clarified by determining the values of ξ_{loc} and R_{hop} as a function of T (equation 6 and Methods). Figure 5d shows that $\xi_{loc,GR} \approx 13$ nm (red circles) is nearly independent of T and much larger than that in MoS$_2$ devices, consistent with the more conductive behaviour of graphene devices. Also, $R_{hop,GR}$ shows a non-monotonic temperature dependence (Fig. 5d, red diamonds): for $T < 40$ K, $R_{hop,GR}$ slightly decreases with increasing T, going from ~16 to ~13 nm; for $T > 40$ K instead, it slowly increases, reaching ~20 nm close to room temperature. This behaviour can be ascribed to the fact that, in this case, $T_{0,GR}$ is smaller than room temperature and the factor F_0 in equation (7) (Methods) becomes relevant as T approaches and exceeds $T_{0,GR}$. Most importantly, in graphene devices, $R_{hop,GR}$ is systematically larger than the average flake thickness $t_{av,GR}$ for any T, consistent with carrier hopping primarily occurring between different graphene flakes in the 3D network. These results are confirmed by measuring the magnetoresistance ratio MR $= [\rho(B) - \rho(0)]/\rho(0)$, which directly probes ξ_{loc} in the VRH regime[80] (Methods). Here $\rho = \sigma^{-1}$ is the resistivity of our graphene device and B is the magnetic field. Figure 5c shows the experimental values of MR as a function of B (symbols), measured with B in the

out-of-plane direction at temperatures between 4.2 and 40.1 K; the solid lines represent the best fit to our experimental MR data using equation (9) (Methods). The MR is always negative, quasi-linear at low B, with an incipient saturation at high B for $T \leq 20$ K. Such a behaviour is typical of MR in the VRH regime[80], which is determined by the sum of a linear ($\propto B$) and quadratic ($\propto B^2$) contribution arising from the quantum interference of different hopping paths and the contraction of charge-carrier wavefunction at impurity centres, respectively[80]. Our fits with this model show excellent agreement with the experimental data. Figure 5d shows the values of $\xi_{loc,GR}$ (black circles) and $R_{hop,GR}$ (black diamonds) obtained from the best fits of the MR data (Fig. 5c). Both $\xi_{loc,GR}$ and $R_{hop,GR}$ are ~15 nm at 4.3 K and decrease to ~11 and ~13 nm at 40.1 K respectively, in excellent agreement with the values determined from equation (6). Overall, the charge transport in our inkjet-printed graphene devices is, thus, fully described in terms of a Mott VRH conduction process dominated by inter-flake hopping processes, on the verge of an IMT for $T \geq T_{0,GR}$.

Weakly localized transport in inkjet-printed MXene devices

Figure 6a shows ρ as a function of T for a printed MXene device (green curve) as compared with that of a MXene film with similar thickness epitaxially grown on sapphire[63] (black curve). The ρ value of the printed film is about one order of magnitude larger

than that of the epitaxial film ($\rho \approx 47.6$ and $5.86\,\mu\Omega\,m$, respectively, at $T = 290\,K$), indicating that the printed film is more disordered than the epitaxial film. In both cases, ρ depends only weakly on T, in full contrast with the exponential dependence observed in printed graphene and MoS_2 films and in line with the typical behaviour of a disordered metallic system[60–62]. For $T \geq 100\,K$, ρ increases with increasing T, indicating that conduction occurs over extended states when e–ph scattering is activated by increasing T (refs. [60–62]). For $T \leq 100\,K$, ρ exhibits a minimum at $T \approx 80\,K$ and increases again with decreasing T (Fig. 6a). Such a low-T upturn is typical of disordered 2D metals[34,81,82] and was also observed in isolated Ti_3C_2 flakes[35], epitaxial films[63] and spray-casted networks[71], strongly pointing to a common charge transport mechanism in all these systems. A mainly 2D charge transport is rather reasonable in our MXene devices due to the large lateral size and small thickness of the flakes, together with excellent substrate conformality and a narrow distribution of their average relative inclination peaked at $\theta_{max,MX} \approx 0.63°$ (Supplementary Fig. 10).

Figure 6b shows that $\sigma_s = \sigma t_{d,MX}$ (green line) is proportional to $\log(T)$ in the range of $7 \leq T \leq 70\,K$ (dashed line), as usually observed in disordered 2D conductors[34,81,82] or in granular metals where inter- and intra-grain conductances are comparable[62]. However, in the latter case, the experimentally observed fully metallic T dependence for $T \geq 100\,K$ cannot develop[62]. Considering that the same behaviour was observed in isolated flakes[35] and epitaxial films[63] and that the ratio (η) of the proportional change of $d\rho/dT$ to the proportional change in ρ due to gate-induced doping is positive (Supplementary Fig. 13)[71], we, thus, treat our printed MXene devices as granular 2D metals where intra-grain conductance dominates the electronic transport. The logarithmic scaling of σ_s with T can then be due to three distinct phenomena (or a combination thereof)[34,81,82]: Kondo effect, electron–electron interactions and weak localization (WL). Among these, in epitaxial MXene thin films, WL has been proposed to be responsible for the upturn in ρ occurring at low T[63].

These phenomena feature a unique dependence of magneto-conductance $\Delta\sigma(B,T) = \sigma_s(B,T) - \sigma_s(0,T)$ on B due to their distinct physical origin, as detailed in Supplementary Section XVI. Figure 6c shows that at any T between ~4.3 and ~40.0 K, our MXene devices exhibit a finite and positive $\Delta\sigma(B)$ (filled circles), ruling out the B-independent electron–electron interactions as a major source for the ρ upturn[34,81,82]. The $\Delta\sigma(B,T)$ is symmetric for positive and negative values of B (Fig. 6d), but even at $T = 4.2\,K$ (violet circles), it does not follow a quadratic behaviour in the low-field limit ($|B| \leq 2\,T$) and cannot be satisfactorily fitted by a parabola (dashed line); therefore, even the Kondo effect is excluded as a source for the ρ upturn[83]. Figure 6e shows the anisotropic magnetoconductance $AMC = \sigma_s(B,\theta) - \sigma_s(B,0)$, where θ is the angle between B and the substrate plane. At any B, the experimental AMC data (Fig. 6e, filled circles) closely follow the $\sin(\theta)$ dependence expected for a 2D Fermi surface[84] (Fig. 6e, solid lines), and the positive $\Delta\sigma(B,T)$ observed on the application of an out-of-plane B ($\theta = 90°$) is entirely suppressed when B is applied in plane ($\theta = 0°$), as expected in the case of the 2D WL behaviour[34,81,82] (Supplementary Fig. 14). Consistent with the findings on epitaxial MXene films[63], we, thus, attribute the source of ρ upturn below T $\approx 80\,K$ to the presence of 2D WL, and quantitatively analyse our data employing the Hikami–Larkin–Nagaoka model[85] (Methods). The fits of the experimental $\Delta\sigma(B,T)$ values to equation (12) (Fig. 6c, solid lines) are in agreement with the experimental values of $\Delta\sigma(B)$ for all the values of T. Charge transport in our MXene devices is, thus, well described in terms of WL in the presence of a finite spin–orbit interaction (SOI), with no qualitative differences with respect to what found on epitaxial films[63].

Figure 6f shows the phase-coherence length L_ϕ (red diamonds), spin–orbit length L_{so} (black circles) and elastic scattering length L_e (green pentagons) determined from the fits in Fig. 6c (Methods). Here $L_e \approx 10\,nm$ and nearly independent of T for $T \leq 10\,K$, as expected for

scattering with defects, and is comparable but larger than the mean free path of ~2 nm estimated at 300 K (ref. [45]), the latter reduced by e–ph scattering. Also, L_ϕ decreases with increasing T and scales as $T^{-1/2}$ (Fig. 6g), identifying Nyquist electron–electron scattering as the main source of dephasing in the system[34,86]. Furthermore, L_{so} is constant with T, as typical for 2D conductors with finite SOI[86]; it is larger than both L_ϕ and L_e at any T, indicating that SOI is unable to induce a complete spin precession in the charge carriers before they lose phase coherence. This would destroy the constructive interference responsible for WL and lead to the appearance of weak anti-localization. However, no weak-anti-localization-induced negative magnetoconductance close to $B = 0$ is observed in Fig. 6c,d, in agreement with the results on MXene epitaxial films[63]. Moreover, at $T = 4.3\,K$, L_ϕ approaches L_{so}, accounting for the incipient saturation of σ_s observed for $T \leq 7\,K$ due to the reduced constructive interference (Supplementary Section XVI). Since L_ϕ, L_{so} and L_e remain much smaller than the average lateral size of MXene flakes, the WL behaviour in our printed MXene devices is fully determined by phase-coherent intra-flake charge transport.

Conclusions

We have reported the charge transport mechanisms of inkjet-printed thin-film field-effect devices made from semiconducting (MoS_2), semimetallic (graphene) and metallic (MXene Ti_3C_2) few-layer E2D inks. We investigated their electrical conductivity as a function of temperature, magnetic field and gate voltage, accounting for morphological features of the flakes and printed films. We showed that charge transport in printed MoS_2 and MXene devices is dominated by the intrinsic intra-flake processes, leading to a temperature-induced crossover between 3D Mott VRH and NNH in the former and a weakly localized metallic behaviour in the latter. In the printed graphene devices, charge transport is determined by inter-flake processes, leading to a VRH behaviour up to room temperature in spite of the semimetallic nature of single flakes and resulting in a strong dependence of the dimensionality of charge transport on that of the flake network in the printed film. Our findings establish the mechanisms responsible for charge transport in inkjet-printed devices made of E2D inks and could lead to the reliable design of more complex printed electronics with E2D inks.

Methods

Graphene-ink preparation. The graphene ink was prepared by the surfactant-free liquid-phase exfoliation of graphite using a high-boiling-point solvent that was then solvent-exchanged into a low-boiling-point solvent, thus minimizing solvent residuals. The use of a low-boiling-point solvent aids to prevent the coffee-ring effect, thus creating a uniform film. In addition, we used a low-boiling-point solvent that is non-toxic and does not damage the inkjet-printer cartridge (piezoelectric-based printhead) during the printing process. An initial 1.5 g graphite (Sigma-Aldrich no. 332461; size, <100 μm) was added to 150 ml of N-Methyl-2-pyrrolidone (NMP) and ultrasonicated (Fisherbrand FB15069; maximum power, 800 W) for 9 h. The graphite–NMP ink was subsequently centrifugated (Sorvall WX 100 mounting a TH-641 swinging-bucket rotor) for 1 h at 10,000 r.p.m. The supernatant was transferred into a clean glass bottle using a micropipette. Great care was taken during pipetting to avoid the disturbance of the sediment layer that could redisperse into the supernatant. Solvent exchange was carried out via vacuum filtration, where 20 ml graphene ink was passed through a polytetrafluoroethylene (PTFE) membrane (Merck Millipore, 0.1 μm). Graphene collected on the PTFE membrane was transferred to a small vial along with 5 ml pure ethanol. This was followed by 10 min of ultrasonication. Printing was immediately carried out after ink preparation.

Ti₃C₂ (MXene)-ink preparation. The MXene ink was prepared by following the mild-exfoliation-route protocol for the MAX phase powder (Ti_3AlC_2; Carbon-Ukraine). This involves etching the Al atom in the MAX powder via the creation of in situ hydrofluoric acid. As for the graphene ink, we also opted for the solvent-exchange route for the MXene ink by exchanging the high-boiling-point solvent to a benign low-boiling-point solvent. In a vented 40 ml PTFE vessel, deionized water (5 ml) was added, followed by the drop-wise addition of concentrated hydrochloric acid (15 ml; Sigma). Lithium fluoride (LiF) powder (1 g, Sigma) was added to the resultant 9 M hydrogen chloride (HCl), and the vessel was then immersed in a mineral oil bath at 35 °C and stirred using a magnetic PTFE

bar for 10 min to fully dissolve the LiF and allow the temperature to stabilize. The Ti_3AlC_2 MAX phase powder (1 g) was then added in small amounts to the vessel to avoid overheating the solution. The solution was then stirred for 24 h to obtain the etched multilayer $Ti_3C_2T_x$ MXene. The contents of the vessel were transferred into a 50 ml centrifuge tube and diluted to a total of 40 ml with deionized water. The dispersion was then sedimented via centrifugation at 5,000 r.p.m. using a Thermo Scientific Heraeus Multifuge X1 for 5 min, discarding the supernatant and repeating several times, until the pH of the supernatant was 6. To delaminate the washed multilayer MXene, the tube was tightly sealed and vigorously shaken by hand and vortex-mixed for 30 min. The dispersion was then centrifuged at 1,500 r.p.m. for 30 min to sediment any many-layer MXenes or unreacted MAX phases. The supernatant containing the delaminated MXene flakes was then collected. For ease of printing, the dispersion was transferred into NMP (Sigma-Aldrich) via centrifugation at 5,000 r.p.m., redispersing the sediments in minimal NMP and repeating three times to remove the remaining water. To obtain a printable MXene dispersion in ethanol, the NMP ink was transferred via centrifugation and repeating three times with absolute ethanol (5 ml; Fisher Scientific). The resulting dispersion was sonicated for 15 min to break up the agglomerated flakes and then centrifuged at 2,500 r.p.m. for 30 min to remove any remaining agglomerates. The supernatant was collected for use in inkjet printing.

MoS_2-ink preparation. The MoS_2 ink was prepared by following the electrochemical exfoliation route that involved the intercalation of quaternary ammonium bromide in between the bulk MoS_2 layers. The electrochemical set up involved the use of a natural MoS_2 crystal (HQ graphene) and a graphite rod (Qingdao Tennry Carbon) as the cathode and anode, respectively. The electrolyte was made by adding 0.2 g quaternary ammonium bromide (Sigma-Aldrich; CAS no. 4368-51-8; SKU, 87301) to 40 ml acetonitrile, giving a concentration of 5 mg ml^{-1}. Both MoS_2 crystal and graphite electrode were submerged in the quaternary ammonium bromide electrolyte and the applied voltage was set at 8 V for 1 h. The expanded MoS_2 crystal was washed with ethanol and then broken up into smaller pieces. The small pieces of MoS_2 were transferred to a test tube and dimethylformamide with polyvinylpyrrolidone (22 mg ml^{-1}; Sigma-Aldrich, CAS no. 9003-39-8; SKU, PVP40; molecular weight, 40,000) was added to the test tube; the mixture was sonicated for 30 min. The mixture was then broken down further using a shear mixer (IKA T 10). The dispersion was then centrifuged at 3,000 r.p.m. for 20 min to remove any large pieces of MoS_2 that were not electrochemically exfoliated. The supernatant was then centrifuged again at 5,000 r.p.m. for 10 min to further separate the few-layer MoS_2 flakes from bulk MoS_2. Both centrifugation steps were performed using a ProteomeLab XL-A (Beckman Coulter) along with an SW 32 Ti swinging-bucket rotor. The supernatant of the second centrifugation step was placed under a vacuum line (~1 mbar) to remove the dimethylformamide solvent and concentrate the MoS_2 ink. The concentrated dispersion (volume, 10 ml) was centrifuged at 45,000 r.p.m. for 30 min to sediment the MoS_2 flakes. This centrifuge step was performed using a Beckman Optima MAX ultracentrifuge. The sediment MoS_2 was redispersed in isopropyl alcohol with polyvinylpyrrolidone (22 mg ml^{-1}). The MoS_2 dispersed in isopropyl alcohol was directly used to print the MoS_2 film with no further processing required.

TEM. TEM was performed using an FEI Philips Tecnai F-20 instrument operated at 200 kV (Schottky field-emission gun) with a line resolution of 0.10 nm and point resolution of 0.24 nm. The TEM sample was prepared by diluting the initial E2D ink by a factor of 100 and drop casting the diluted solution on a holey carbon film with a 400 mesh copper (Cu) grid that was then allowed to dry in ambient air overnight.

Inkjet printing. Before performing the printing process, each Si/SiO$_2$ substrate (Graphene Supermarket; 285 nm and p-doped) was treated with ozone plasma (NanoBioAnalytics UV Ozone Cleaner UVC-1014) to make the surface more hydrophilic. A drop-on-demand inkjet printer (Fujifilm Dimatix DMP-2800) with a nozzle diameter of 21 μm that produces droplets with a volume of ~10 pl was used to print the devices. The E2D inks were made using low-boiling-point solvents (<100 °C) that evaporate at room temperature and hence minimize both transport of particulates (causing the coffee-ring effect) and material redispersion, thus improving the morphological uniformity of the film.

Rheology. A rotational rheometer (Discovery Hybrid Rheometer HR-1), which uses a parallel-plate method to measure the viscosity and viscoelastic properties of a liquid, was used to characterize all the inks employed in this work. Shear thinning was observed in all the inks. The surface tension of the inks was measured using the pendant drop method (First Ten Angstroms FTA1000B). Built-in software analysed the shape of the suspended droplet formed at the end of the needle via drop shape analysis. Ink density (ρ) was measured by weighing 1 ml ink on a microbalance (Sartorius ME5). The density of inks was determined as $\rho = m/V$, where m and V are the mass and volume, respectively. All the inks were formulated with surface tension $\gamma \approx 29$ mN m^{-1} and viscosity $\eta \approx 1$ mPa (Supplementary Figs. 5 and 6). The corresponding density of inks is $\rho_{GR} \approx 0.80$ g cm^{-3}, $\rho_{MS} \approx 0.70$ g cm^{-3} and $\rho_{MX} \approx 0.99$ g cm^{-3} for the graphene, MoS_2 and MXene inks, respectively. The Ohnesorge number (a dimensionless number that relates the viscous forces to

inertial and surface tension forces) was determined as $Oh = \eta / \sqrt{\rho \gamma L}$, where L is the diameter of the nozzle, and the corresponding figure of merit $Z = Oh^{-1}$ was derived.

Optical absorption spectroscopy. The flake concentration c of graphene, MXene and MoS_2 inks was determined using the Beer–Lambert law: $A = \alpha c l$, where c is the concentration, l is the beam path length and α is the absorption coefficient. For α, we used the values at 660 nm as $\alpha_{660(GR)} \approx 2,460$ l g^{-1} m^{-1} for the graphene ink[12], $\alpha_{660(MX)} \approx 538$ l g^{-1} m^{-1} for the MXene ink (Supplementary Fig. 15) and $\alpha_{672(MS)} \approx 3,400$ l g^{-1} m^{-1} for the MoS_2 ink.

Raman spectroscopy. A Renishaw 1000 InVia micro-Raman spectrometer was used to acquire the Raman spectra. The spectra shown in Fig. 2 were measured using a 514 nm laser with ×20 objective. All the Raman spectra were acquired using a laser power of ~1 mW.

AFM. The inks were diluted by a factor of 100 and then drop casted onto pieces of Si/SiO$_2$ wafers and allowed to dry in ambient air. A short annealing step of 1 min at the boiling temperature of the solvent used to make the E2D ink was performed before acquiring the AFM images. AFM measurements were performed using a Bruker Dimension Icon in the PeakForce mode using a silicon tip on a nitride lever.

XPS data of graphene and MoS_2 inks. A K-Alpha$^+$ surface analyser by Thermo Scientific was used to carry out measurements on all the inkjet-printed devices on SiO$_2$. A spot size of 200−400 μm was used for all the samples. The spectra were obtained in a vacuum at a pressure of $<8 \times 10^{-7}$ mbar. The system employs a microfocused Al Kα X-ray source (1,486 eV) and a 2D detector attached to a 180° double-focusing hemispherical analyser. Further analysis of the XPS data was carried out using the Avantage software (Thermo Scientific).

XPS data of Ti_3C_2 ink. XPS data were recorded from an Omicron EA 125 energy analyser (Scienta Omicron) using an XM1000 monochromated Al K X-ray source. The instrument's base pressure was 2×10^{-10} mbar and the instrument resolution was 0.6 eV. The spectra were deconvoluted and fitted using CasaXPS (Casa Software).

Device fabrication. All the E2D-ink devices were produced using 25 printing passes. In the printed MoS_2 devices, we submerge our devices in bis(trifluoromethane) sulfonimide and 1,2-dichloroethane at 100 °C for 1 h. The treatment is performed in a nitrogen glovebox to avoid exposing bis(trifluoromethane)sulfonimide to moisture in the ambient atmosphere[66]. The devices are then annealed at 400 °C for 1 h to remove any residual solvent. We then created a thin gate oxide suitable for electric-field modulation. Electron-beam lithography was used to pattern ~1-mm-long source, drain and gate electrodes on the Si/SiO$_2$ substrate. We use Ti/Au (5/35 nm) for the source and drain electrodes and Al (40 nm) for the gate electrodes of the FET. A thin native AlO$_x$ layer was formed at the top surface of Al by air exposure (gate length, ~600 nm; width, ~400 μm).

Charge transport measurements. The electrical connections for charge transport measurements were realized by placing thin Au wires on the SiO$_2$/Si substrates close to the printed devices and then drop casting small (~100 μm) droplets of electrically conductive silver paste (RS Components). Temperature-dependent charge transport measurements were performed in the high-vacuum chamber of a Cryomech pulse-tube cryocooler with a base temperature of 2.8 K. Magnetic-field-dependent measurements were performed in a helium atmosphere in the variable-temperature insert of an Oxford Instruments ^{4}He cryostat equipped with a 9 T superconducting magnet. The conductivity of the printed devices was determined as

$$\sigma = \frac{l}{w t_d} \frac{I}{V}, \tag{3}$$

where l is the channel length, w is the channel width, t_d is the device thickness, I is the current flowing through the channel and V is the voltage drop across the channel. The nearly linear scaling of σ_{GR} and σ_{MX} with V_G for both graphene and MXene printed devices (Supplementary Fig. 7) at any T for $|V_G| \le 40$ V allowed to determine the field-effect mobility μ_{FE} in both devices as

$$\mu_{FE} = \frac{t_d}{C_G} \left| \frac{\partial \sigma}{\partial_G} \right| \tag{4}$$

and the average density of free carriers per unit volume at $V_G = 0$, $n_{3D}|_0$, as

$$n_{3D}|_0 = \frac{\sigma(V_G = 0)}{e \, \mu_{FE}}, \tag{5}$$

where e is the elementary charge; $C_G = \varepsilon_{ox}\varepsilon_0/t_{ox}$ is the gate capacitance per unit area; ε_0 is the vacuum permittivity; and ε_{ox} and t_{ox} are the dielectric constant

and thickness of the gate oxide, respectively. For the printed MXene and graphene devices, $t_{ox} = 285$ nm and $\varepsilon_{ox} = 3.9$ is the permittivity of SiO_2 (ref. [29]), resulting in $C_G = 12.1$ nF cm^{-2}. For the printed MoS_2 devices, $t_{ox} \approx 37$ nm and $\varepsilon_{ox} \approx 3.77$ as an effective-medium approximation of AlO_x and vacuum, resulting in $C_G \approx 95$ nF cm^{-2} (details provided elsewhere[66]). For ion-gated MoS_2 devices, the same definition of μ_{FE} is employed, except that the solid-oxide capacitance is substituted for the ionic-gate capacitance $C_G \approx 10.8$ μF cm^{-2} determined by low-bias cyclic voltammetry[87] (Supplementary Section XIX and Supplementary Fig. 16). Additionally, the two clearly different slopes in the plot of σ_{MS} as a function of V_G observed in the ion-gated MoS_2 devices above and below $V_G \approx 1.37$ V require a separate determination of $\mu_{FE,MS}$ for these two cases in the temperature range from 300 to 220 K. Only one gate has been used on MoS_2 devices at a time.

The printed MXene and graphene devices were measured in the four-probe configuration by supplying a small constant current $I_D \approx 1$ μA between the outer drain and source contacts with a two-channel Agilent B2912 source measure unit (SMU) and determining the longitudinal voltage drop V_{xx} between the inner voltage contacts with an Agilent 34420 nanovoltmeter. Common-mode offsets were removed by the current reversal method. The gate voltage of $-80 \leq V_G \leq +80$ V was applied between the source contact and p-doped Si back gate with the same two-channel SMU. The printed MoS_2 devices were too resistive for the four-probe method to be reliable and were thus measured in the two-probe configuration with a Keithley 2636B SMU by linearly sweeping V_D from -0.1 to $+0.1$ V, measuring the resulting I_D and performing a linear fit to the data. All the measured $I–V$ curves in the printed MoS_2 devices show a linear behaviour, indicating ohmic contacts to the sample, and the contact resistance was determined to be negligible with respect to the total resistance of the device (Supplementary Fig. 17). In the printed MoS_2 devices in the absence of the ionic gate, $-1.5 \leq V_G \leq +1.5$ V was applied to the Al/AlO_x gate and an effective width w equal to 10% of the apparent one was employed in the calculations owing to the conductive AFM measurements, indicating that only a 10% fraction of the MoS_2 flakes were electrically connected to the Au leads. When the ionic gate was applied, we tuned σ_{MS} at low T by scanning V_G in 0.125 V steps between 0 and 2 V. At each step, a waiting time of ~10 min minimized the influence of diffusion dynamics of the ions inside the MoS_2 film. We recorded the T dependence of σ_{MS} between 300 and 220 K, below which the channel integrity was compromised due to the freezing of the ionic liquid.

Calculation of localization and average hopping lengths. For 3D Mott VRH, the localization length ξ_{loc} is related to the characteristic temperature T_0 as[60,61]

$$T_0 = \frac{24}{\pi k_B N(E_F) \xi_{loc}^3}, \tag{6}$$

where $N(E_F)$ is the DOS at the Fermi level E_F and the average hopping length R_{hop} is simply[60,75]

$$R_{hop} = \frac{3}{8} \left(\frac{T_0}{T} \right)^{\frac{1}{4}} \xi_{loc} F_0, \tag{7}$$

where F_0 is a correction factor that describes the VRH regimes when the condition $T \ll T_0$ is not satisfied (Supplementary Fig. 18a).

For our printed MoS_2 devices, from the fit of the curve (Fig. 4a) to equation (1) with $p = 1/4$, we obtain $T \ll T_{0,MS} = (3.07 \pm 0.10) \times 10^6$ K in the ungated case, resulting in $F_0 = 1$. Then, $N(E_F)_{MS}$ can be obtained from $E_{a,MS}$ in the NNH regime at $V_G = 0$ ($E_{a,MS} = 96.1 \pm 0.5$ meV) since $E_a^{-1} = N(E_F)a^3$ (ref. [60]), where a is the minimum distance between the hopping sites. From the statistics of the Raman spectra of the printed MoS_2 flakes (Supplementary Fig. 19), we determine the inter-defect length L_D and thus set $a = L_D \approx 1.54$ nm, in good agreement with previous reports ($a \approx 1.7$ nm (ref. [31])).

Since the printed graphene devices do not exhibit NNH behaviour in any temperature range, $N(E_F)_{GR}$ cannot be estimated by starting from the activation energy of NNH; rather, one can estimate $N(E_F)_{GR}$ by combining the average free carrier density per unit volume $n_{3D}|_{0,GR}$ (Supplementary Fig. 8a) with the energy dependence of DOS in graphite as determined by ab initio density functional theory[88]:

$$n_{3D}|_0 = \int_{E_D}^{E_F} N(E) dE, \tag{8}$$

where E_D is the energy of the Dirac point. The validity of this approach in our graphene devices can be confirmed by independently determining ξ_{loc} from the magnetic-field dependence of their resistivity, since measuring the magnetoresistance of a material in the VRH regime allows the direct probing of ξ_{loc} without having to make any assumption on its DOS[80]. As discussed below, in the case of 3D Mott VRH and in the low-magnetic-field limit ($B \ll B_{sat}, B_c$) the magnetoresistance ratio $MR = [\rho(B) - \rho(0)]/\rho(0)$ takes a specific field dependence given by equation (9), containing ξ_{loc} as a parameter.

Magnetoresistance and magnetoconductance fits. The magnetoresistance curves of the printed graphene device (Fig. 5e) were fitted to the standard expression for hopping transport[80] as

$$MR = -C_{sat} \frac{B}{B_{sat}} + t^2 \frac{B^2}{B_c^2}. \tag{9}$$

Here B_{sat} and B_c are the characteristic values of B related to localization length ξ_{loc}:

$$B_{sat} = 0.7 \left(\frac{8}{3} \right)^{\frac{3}{2}} \left(\frac{2\pi\hbar}{e\xi_{loc}^2} \right) \left(\frac{T}{T_0} \right)^{\frac{3}{8}}, \tag{10}$$

$$B_c = \frac{6\hbar}{e\xi_{loc}^2} \left(\frac{T}{T_0} \right)^{\frac{3}{8}}, \tag{11}$$

where C_{sat} is the positive saturation constant[80], $t^2 = 0.0893$ is a numerical coupling constant[80] and $\hbar$ is the reduced Planck constant. The corresponding values of B_{sat} and B_c were found to be always larger than 17 and 8 T, respectively, validating the choice of the low-magnetic-field limit.

Conversely, the magnetoconductance curves of the printed MXene device (Fig. 6) were fitted to the Hikami–Larkin–Nagaoka model, which describes the magnetoconductance of 2D metallic systems in the presence of finite intrinsic SOI[86]:

$$\Delta\sigma(B) = \frac{e^2}{2\pi^2\hbar} \left[F\left(\frac{B_\phi}{B} \right) \right] + \frac{e^2}{2\pi^2\hbar} \left[F\left(\frac{B_{so}+B_e}{B} \right) \right] \\ - \frac{3e^2}{2\pi^2\hbar} \left[F\left(\frac{(4/3)B_{so}+B_\phi}{B} \right) \right] \tag{12}$$

with

$$F(z) = \ln(z) - \psi(1/2 + z) \tag{13}$$

and

$$B_{\phi,so,e} = \hbar/4eL_{\phi,so,e}^2, \tag{14}$$

where ψ is the digamma function[34].

The magnetic-field-dependent charge transport data shown in Figs. 5e and 6e were fitted to equation (9) and equation (12), respectively, using a Levenberg–Marquardt algorithm implemented in the OriginLab software. In both cases, the curve measured at the lowest T, being most sensitive to the fit parameters, was fitted first, and the uncertainties were automatically determined by the software. The best-fit parameters of the curve were then used as the initial guesses for the fit to the next curve at larger T, and the procedure was repeated at all the values of T. At high T, the experimental curves were sometimes too smooth for the fits to converge, due to mutual dependency between the free parameters. In this case, multiple fits were performed by fixing one parameter at a time, whereas the other parameters were left free. The final values of the parameters were then obtained by averaging the results and the uncertainties determined by their maximum differences.

Data availability

The data that support the findings of this study are available at https://data.hpc.imperial.ac.uk/ and from the corresponding author upon reasonable request.

References

1. Torrisi, F. & Carey, T. Graphene, related two-dimensional crystals and hybrid systems for printed and wearable electronics. *Nano Today* **23**, 73–96 (2018).
2. Torrisi, F. & Coleman, J. N. Electrifying inks with 2D materials. *Nat. Nanotechnol.* **9**, 738–739 (2014).
3. Carey, T. et al. Fully inkjet-printed two-dimensional material field-effect heterojunctions for wearable and textile electronics. *Nat. Commun.* **8**, 1202 (2017).
4. Kelly, A. G. et al. All-printed thin-film transistors from networks of liquid-exfoliated nanosheets. *Science* **356**, 69–73 (2017).
5. Li, J., Naiini, M. M., Vaziri, S., Lemme, M. C. & Östling, M. Inkjet printing of MoS_2. *Adv. Funct. Mater.* **24**, 6524–531 (2014).
6. Karagiannidis, P. G. et al. Microfluidization of graphite and formulation of graphene-based conductive inks. *ACS Nano* **11**, 2742–2755 (2017).
7. Ren, J. et al. Environmentally-friendly conductive cotton fabric as flexible strain sensor based on hot press reduced graphene oxide. *Carbon* **111**, 622–630 (2017).

8. Qiang, S. et al. Wearable solid-state capacitors based on two-dimensional material all-textile heterostructures. *Nanoscale* **11**, 9912–9919 (2019).

9. Parvez, K. et al. Exfoliation of graphite into graphene in aqueous solutions of inorganic salts. *J. Am. Chem. Soc.* **136**, 6083–6091 (2014).

10. Lin, Z. et al. Solution-processable 2D semiconductors for high-performance large-area electronics. *Nature* **562**, 254–258 (2018).

11. Paton, K. R. et al. Scalable production of large quantities of defect-free few-layer graphene by shear exfoliation in liquids. *Nat. Mater.* **13**, 624–630 (2014).

12. Hernandez, Y. et al. High-yield production of graphene by liquid-phase exfoliation of graphite. *Nat. Nanotechnol.* **3**, 563–568 (2008).

13. Hasan, T. et al. Solution-phase exfoliation of graphite for ultrafast photonics. *Phys. Stat. Sol. (B)* **247**, 2953–2957 (2010).

14. Coleman, J. N. et al. Two-dimensional nanosheets produced by liquid exfoliation of layered materials. *Science* **331**, 568–571 (2011).

15. Torrisi, F. et al. Inkjet-printed graphene electronics. *ACS Nano* **6**, 2992–3006 (2012).

16. Kumar, D. K. et al. Scalable screen-printing manufacturing process for graphene oxide platinum free alternative counter electrodes in efficient dye sensitized solar cells. *FlatChem* **15**, 100105 (2019).

17. Baker, J., Deganello, D., Gethin, D. T. & Watson, T. M. Flexographic printing of graphene nanoplatelet ink to replace platinum as counter electrode catalyst in flexible dye sensitised solar cell. *Mater. Res. Innov.* **18**, 86–90 (2014).

18. Carey, T., Jones, C., Le Moal, F., Deganello, D. & Torrisi, F. Spray-coating thin films on three-dimensional surfaces for a semitransparent capacitive-touch device. *ACS Appl. Mater. Interfaces* **10**, 19948–19956 (2018).

19. Sarycheva, A. et al. 2D titanium carbide (MXene) for wireless communication. *Sci. Adv.* **4**, eaau0920 (2018).

20. Zhang, C. J. et al. Additive-free MXene inks and direct printing of micro-supercapacitors. *Nat. Commun.* **10**, 1795 (2019).

21. Finn, D. J. et al. Inkjet deposition of liquid-exfoliated graphene and MoS_2 nanosheets for printed device applications. *J. Mater. Chem. C* **2**, 925–932 (2014).

22. Micallef, F. G. et al. Transparent conductors for mid-infrared liquid crystal spatial light modulators. *Thin Solid Films* **660**, 411–420 (2018).

23. Bianchi, V. et al. Terahertz saturable absorbers from liquid phase exfoliation of graphite. *Nat. Commun.* **8**, 15763 (2017).

24. Wang, F. et al. Graphene passively Q-switched two-micron fiber lasers. In *2012 Conference on Lasers and Electro-Optics (CLEO)* 1–2 (IEEE, 2012).

25. Singh, M., Haverinen, H. M., Dhagat, P. & Jabbour, G. E. Inkjet printing—process and its applications. *Adv. Mater.* **22**, 673–685 (2010).

26. Seo, J.-W. T. et al. Fully inkjet-printed, mechanically flexible MoS_2 nanosheet photodetectors. *ACS Appl. Mater. Interfaces* **11**, 5675–5681 (2019).

27. Ferrari, A. C. et al. Science and technology roadmap for graphene, related two-dimensional crystals, and hybrid systems. *Nanoscale* **7**, 4598–4810 (2015).

28. Xue, J., Huang, S., Wang, J.-Y. & Xu, H. Q. Mott variable-range hopping transport in a MoS_2 nanoflake. *RSC Adv.* **9**, 17885–17890 (2019).

29. Piatti, E. et al. Multi-valley superconductivity in ion-gated MoS_2 layers. *Nano Lett.* **18**, 4821–4830 (2018).

30. Wu, C.-L. et al. Gate-induced metal–insulator transition in MoS_2 by solid superionic conductor LaF_3. *Nano Lett.* **18**, 2387–2392 (2018).

31. Qiu, H. et al. Hopping transport through defect-induced localized states in molybdenum disulphide. *Nat. Commun.* **4**, 2642 (2013).

32. Chen, J.-H., Jang, C., Xiao, S., Ishigami, M. & Fuhrer, M. S. Intrinsic and extrinsic performance limits of graphene devices on SiO_2. *Nat. Nanotechnol.* **3**, 206–209 (2008).

33. Park, C.-H. et al. Electron–phonon interactions and the intrinsic electrical resistivity of graphene. *Nano Lett.* **14**, 1113–1119 (2014).

34. Gonnelli, R. S. et al. Weak localization in electric-double-layer gated few-layer graphene. *2D Mater.* **4**, 035006 (2017).

35. Miranda, A., Halim, J., Barsoum, M. W. & Lorke, A. Electronic properties of freestanding $Ti_3C_2T_x$ MXene monolayers. *Appl. Phys. Lett.* **108**, 033102 (2016).

36. Lipatov, A. et al. Effect of synthesis on quality, electronic properties and environmental stability of individual monolayer Ti_3C_2 MXene flakes. *Adv. Electron. Mater.* **2**, 1600255 (2016).

37. Sangwan, V. K. & Hersam, M. C. Electronic transport in two-dimensional materials. *Annu. Rev. Phys. Chem.* **69**, 299–325 (2018).

38. Akinwande, D. Two-dimensional materials: printing functional atomic layers. *Nat. Nanotechnol.* **12**, 287–288 (2017).

39. Kravets, V. G. et al. Spectroscopic ellipsometry of graphene and an exciton-shifted van Hove peak in absorption. *Phys. Rev. B* **81**, 155413 (2010).

40. Eda, G. et al. Photoluminescence from chemically exfoliated MoS_2. *Nano Lett.* **11**, 5111–5116 (2011).

41. Wilcoxon, J. P., Newcomer, P. P. & Samara, G. A. Synthesis and optical properties of MoS_2 and isomorphous nanoclusters in the quantum confinement regime. *J. Appl. Phys.* **81**, 7934–7944 (1997).

42. Hu, M. et al. Surface functional groups and interlayer water determine the electrochemical capacitance of $Ti_3C_2T_x$ MXene. *ACS Nano* **12**, 3578–3586 (2018).

43. Hope, M. A. et al. NMR reveals the surface functionalisation of Ti_3C_2 MXene. *Phys. Chem. Chem. Phys.* **18**, 5099–5102 (2016).

44. Satheeshkumar, E. et al. One-step solution processing of Ag, Au and Pd@ MXene hybrids for SERS. *Sci. Rep.* **6**, 32049 (2016).

45. Dillon, A. D. et al. Highly conductive optical quality solution-processed films of 2D titanium carbide. *Adv. Funct. Mater.* **26**, 4162–4168 (2016).

46. El-Demellawi, J. K., Lopatin, S., Yin, J., Mohammed, O. F. & Alshareef, H. N. Tunable multipolar surface plasmons in 2D $Ti_3C_2T_x$ MXene flakes. *ACS Nano* **12**, 8485–8493 (2018).

47. Hantanasirisakul, K. & Gogotsi, Y. Electronic and optical properties of 2D transition metal carbides and nitrides (MXenes). *Adv. Mater.* **30**, 1804779 (2018).

48. Liu, G. et al. Surface modified Ti_3C_2 MXene nanosheets for tumor targeting photothermal/photodynamic/chemo synergistic therapy. *ACS Appl. Mater. Interfaces* **9**, 40077–40086 (2017).

49. Hoath, S. D. *Fundamentals of Inkjet Printing: The Science of Inkjet and Droplets* (John Wiley & Sons, 2016).

50. Kang, R. et al. Enhanced thermal conductivity of epoxy composites filled with 2D transition metal carbides (MXenes) with ultralow loading. *Sci. Rep.* **9**, 9135 (2019).

51. Schier, V., Michel, H.-J. & Halbritter, J. ARXPS-analysis of sputtered TiC, SiC and $Ti_{0.5}Si_{0.5}C$ layers. *Fresenius J. Anal. Chem.* **346**, 227–232 (1993).

52. García-Romeral, N., Keyhanian, M., Morales-García, Á. & Illas, F. Relating X-ray photoelectron spectroscopy data to chemical bonding in MXenes. *Nanoscale Adv.* **3**, 2793–2801 (2021).

53. Natu, V. et al. A critical analysis of the X-ray photoelectron spectra of $Ti_3C_2T_z$ MXenes. *Matter* **4**, 1224–1251 (2021).

54. Myhra, S., Crossley, J. A. A. & Barsoum, M. W. Crystal-chemistry of the Ti_3AlC_2 and Ti_4AlN_3 layered carbide/nitride phases—characterization by XPS. *J. Phys. Chem. Solids* **62**, 811–817 (2001).

55. Ferrari, A. C. & Basko, D. M. Raman spectroscopy as a versatile tool for studying the properties of graphene. *Nat. Nanotechnol.* **8**, 235–246 (2013).

56. Secor, E. B., Ahn, B. Y., Gao, T. Z., Lewis, J. A. & Hersam, M. C. Rapid and versatile photonic annealing of graphene inks for flexible printed electronics. *Adv. Mater.* **27**, 6683–6688 (2015).

57. Parkin, W. M. et al. Raman shifts in electron-irradiated monolayer MoS_2. *ACS Nano* **10**, 4134–4142 (2016).

58. Acerce, M., Voiry, D. & Chhowalla, M. Metallic 1T phase MoS_2 nanosheets as supercapacitor electrode materials. *Nat. Nanotechnol.* **10**, 313–318 (2015).

59. De, S., King, P. J., Lyons, P. E., Khan, U. & Coleman, J. N. Size effects and the problem with percolation in nanostructured transparent conductors. *ACS Nano* **4**, 7064–7072 (2010).

60. Mott, N. F. & Davis, E. A. *Electronic Processes in Noncrystalline Materials* (Oxford Univ. Press, 1979).

61. Mott, N. F. *Metal-Insulator Transition* (Taylor & Francis, 1990).

62. Beloborodov, I. S., Lopatin, A. V., Vinokur, V. M. & Efetov, K. B. Granular electronic systems. *Rev. Mod. Phys.* **79**, 469 (2007).

63. Halim, J. et al. Transparent conductive two-dimensional titanium carbide epitaxial thin films. *Chem. Mater.* **26**, 2374–2381 (2014).

64. Wang, H., Wu, Y., Cong, C., Shang, J. & Yu, T. Hysteresis of electronic transport in graphene transistors. *ACS Nano* **4**, 7221–7228 (2010).

65. Wang, F. et al. Inter-flake quantum transport of electrons and holes in inkjet-printed graphene devices. *Adv. Funct. Mater.* **31**, 2007478 (2021).

66. Carey, T. et al. Inkjet printed circuits with 2D semiconductor inks for high-performance electronics. *Adv. Electron. Mater.* **7**, 2100112 (2021).

67. Li, G. et al. Equilibrium and non-equilibrium free carrier dynamics in 2D $Ti_3C_2T_x$ MXenes: THz spectroscopy study. *2D Mater.* **5**, 035043 (2018).

68. Emelianova, E. V., Van der Auweraer, M., Adriaenssens, G. J. & Stesmans, A. Carrier mobility in two-dimensional disordered hopping systems. *Org. Electron.* **9**, 29–135 (2008).

69. Ippolito, S. et al. Covalently interconnected transition metal dichalcogenide networks via defect engineering for high-performance electronic devices. *Nat. Nanotechnol.* **16**, 592–598 (2021).

70. Halim, J., et al. Variable range hopping and thermally activated transport in molybdenum-based MXenes. *Phys. Rev. B* **98**, 104202 (2018).

71. Hart, J. L. et al. Control of MXenes' electronic properties through termination and intercalation. *Nat. Commun.* **10**, 522 (2019).

72. Kovtun, A. et al. Multiscale charge transport in van der Waals thin films: reduced graphene oxide as a case study. *ACS Nano* **15**, 2654–2667 (2021).

73. Kim, J. S. et al. Electrical transport properties of polymorphic MoS_2. *ACS Nano* **10**, 7500–7506 (2016).

74. Grimaldi, C., Ryser, P. & Strässler, S. Gauge factor of thick-film resistors: outcomes of the variable-range-hopping model. *J. Appl. Phys.* **88**, 4164–4169 (2000).

75. Rodríguez, M., Bonalde, I. & Medina, E. Consistent hopping criterion in the Efros-Shklovskii regime. *Phys. Rev. B* **75**, 235505 (2007).

76. Liu, C.-I. et al. Variable range hopping and nonlinear transport in monolayer epitaxial graphene grown on SiC. *Semicond. Sci. Technol.* **31**, 105008 (2016).

77. Bostwick, A. et al. Quasiparticle transformation during a metal-insulator transition in graphene. *Phys. Rev. Lett.* **103**, 056404 (2009).

78. Elias, D. C. et al. Control of graphene's properties by reversible hydrogenation: evidence for graphane. *Science* **323**, 610–613 (2009).

79. Adkins, C. J., Benjamin, J. D., Thomas, J. M. D., Gardner, J. W. & McGeown, A. J. Potential disorder in granular metal systems: the field effect in discontinuous metal films. *J. Phys. C: Solid State Phys.* **17**, 4633 (1984).

80. Su, T.-I., Wang, C.-R., Lin, S.-T. & Rosenbaum, R. Magnetoresistance of $Al_{70}Pd_{22.5}Re_{7.5}$ quasicrystals in the variable-range hopping regime. *Phys. Rev. B* **66**, 054438 (2002).

81. Ando, T., Fowler, A. B. & Stern, F. Electronic properties of two-dimensional systems. *Rev. Mod. Phys.* **54**, 437 (1982).

82. Beenakker, C. W. J. & van Houten, H. Quantum transport in semiconductor nanostructures. *Solid State Phys.* **44**, 1–228 (1991).

83. Barua, S., Hatnean, M. C., Lees, M. & Balakrishnan, G. Signatures of the Kondo effect in VSe_2. *Sci. Rep.* **7**, 10964 (2017).

84. Pippard, A. B. *Magnetoresistance in Metals* (Cambridge Univ. Press, 1989).

85. Hikami, S., Larkin, A. I. & Nagaoka, Y. Spin-orbit interaction and magnetoresistance in the two dimensional random system. *Prog. Theor. Phys.* **63**, 707–710 (1980).

86. Edmonds, M. T. et al. Spin-orbit interaction in a two-dimensional hole gas at the surface of hydrogenated diamond. *Nano Lett.* **15**, 16–20 (2015).

87. Piatti, E. et al. Ambipolar suppression of superconductivity by ionic gating in optimally doped $BaFe_2(As,P)_2$ ultrathin films. *Phys. Rev. Mater.* **3**, 044801 (2019).

88. Ooi, N., Rajkar, A. & Adams, J. B. Density functional study of graphite bulk and surface properties. *Carbon* **44**, 231–242 (2006).

Author contributions

F.T. designed and directed the project. E.P., D.D. and R.S.G. designed and performed the electriconic transport measurements. A.A. synthesized the graphene and MoS_2 inks, fabricated the devices and performed the UV–vis, AFM, Raman and XPS characterizations. E.P. and A.A. analysed the data. F.G. and L.A. contributed to the transport measurements and data analysis. T.C. contributed to the ink formulation and device fabrication. D.S. synthesised the MXene inks. A.R. and A.Z. performed the XPS characterization and data analysis of the MXene inks. K.A.P. contributed to the device fabrication. F.T. and J.M.K. contributed to the interpretation of Raman, XPS, UV–vis and AFM data. R.S. designed the MoS_2 FET device and analysed the transport data. E.P., A.A., D.D., R.S.G., V.N. and F.T. wrote the manuscript with input from all the authors.

Competing interests

The authors declare no competing interests.

Additional information

Supplementary information The online version contains supplementary material available at https://doi.org/10.1038/s41928-021-00684-9.

Correspondence and requests for materials should be addressed to Felice Torrisi.

Peer review information *Nature Electronics* thanks Lyudmila Turyanska, Jian Zhu and the other, anonymous, reviewer(s) for their contribution to the peer review of this work.

Reprints and permissions information is available at www.nature.com/reprints.

Publisher's note Springer Nature remains neutral with regard to jurisdictional claims in published maps and institutional affiliations.